

Quantifying DNAPL source zone longevity with upscaled modeling: practical insights from flow-cell experiments and uncertainty analyses

Andres Eduardo Prieto Estrada¹, Mark Widdowson², and Lloyd Stewart³

¹Virginia Tech

²Virginia Tech

³Praxis Environmental Technologies, Inc.

December 22, 2022

Abstract

Estimating dissipation timeframes and contaminant mass discharge rates of dense non-aqueous phase liquids (DNAPLs) source zones is of key interest for environmental-management support. Upscaled mathematical modeling of DNAPL dissolution provides a practical approach for assimilating site characterization and downgradient monitoring data to constrain future system behavior. Yet significant uncertainties on predictions of source zone dissipation rates may arise from inadequate or inaccurate conceptual assumptions in parameterization designs. These implications were investigated through upscaled modeling, sensitivity, and uncertainty analyses of high-resolution flow-cell experiments. Sensitivity results emphasized the role of local groundwater velocity and source dimensions in mass transfer scaling by strongly influencing error with respect to DNAPL persistence and dissolution rates. Linear uncertainty analyses, facilitated by PEST ancillary software, demonstrated the worth of monitoring profiles for constraining DNAPL saturations and dispersive mass transfer rates, responsible for source zone longevity. Nonlinear analyses performed with the iterative ensemble smoother PESTPP-iES, facilitated the quantification of unbiased source dissipation uncertainties from DNAPL delineation data. Conversely, monitoring data assimilation without consideration of flow-field heterogeneity and saturation distribution along the flow path biased model predictions. Our analyses provided practical recommendations on upscaled model design to assimilate available site data and support remedial-decision making.

1 Quantifying DNAPL source zone longevity with upscaled modeling: practical 2 insights from flow-cell experiments and uncertainty analyses

3
4 Andres E. Prieto-Estrada¹, Mark A. Widdowson¹, and Lloyd D. Stewart²

5
6 ¹ The Charles E. Via, Jr. Department of Civil and Environmental Engineering, Virginia Tech,
7 Blacksburg, Virginia 24061-0105, United States

8 ² Praxis Environmental Technologies, Inc., 1440 Rollins Road, Burlingame, California 94010,
9 United States

10
11 Corresponding author, e-mail address: mwiddows@vt.edu (M.A. Widdowson)

12 13 Key Points

- 14
15 • Upscaled modeling and uncertainty analyses of flow-cell experiments elucidated upon data
16 assimilation strategies at DNAPL sites
- 17 • Parameterization of source zone heterogeneities for history-matching was necessary to
18 predict unbiased DNAPL dissolution timeframes
- 19 • Coarse DNAPL delineation sufficed to quantify unbiased uncertainty limits of source zone
20 lifespans a priori

21 Abstract

22 Estimating dissipation timeframes and contaminant mass discharge rates of dense non-aqueous
23 phase liquids (DNAPLs) source zones is of key interest for environmental-management support.
24 Upscaled mathematical modeling of DNAPL dissolution provides a practical approach for
25 assimilating site characterization and downgradient monitoring data to constrain future system
26 behavior. Yet significant uncertainties on predictions of source zone dissipation rates may arise
27 from inadequate or inaccurate conceptual assumptions in parameterization designs. These
28 implications were investigated through upscaled modeling, sensitivity, and uncertainty analyses of
29 high-resolution flow-cell experiments. Sensitivity results emphasized the role of local groundwater
30 velocity and source dimensions in mass transfer scaling by strongly influencing error with respect
31 to DNAPL persistence and dissolution rates. Linear uncertainty analyses, facilitated by PEST
32 ancillary software, demonstrated the worth of monitoring profiles for constraining DNAPL
33 saturations and dispersive mass transfer rates, responsible for source zone longevity. Nonlinear
34 analyses performed with the iterative ensemble smoother PESTPP-iES, facilitated the
35 quantification of unbiased source dissipation uncertainties from DNAPL delineation data.
36 Conversely, monitoring data assimilation without consideration of flow-field heterogeneity and
37 saturation distribution along the flow path biased model predictions. Our analyses provided
38 practical recommendations on upscaled model design to assimilate available site data and support
39 remedial-decision making.

40 41 Plain Language Summary

42 Currently, remedial-decision makers rarely benefit from physically-based modeling methods and
43 uncertainty analyses to manage sites impacted by DNAPL source zones. Difficulties in estimating

44 DNAPL dissolution rates stem from source zone heterogeneities, which are difficult to characterize
45 in detail, compounded by a lack of scalable methodologies connecting source zone characterization
46 with discharge monitoring. In addition, monitoring and site characterization efforts supporting
47 performance-based remedial objectives are typically uninformed by uncertainty evaluations
48 predicated on DNAPL mass transfer processes. To bridge that gap, we investigated the impact of
49 data-driven conceptual assumptions on predictions of source zone behavior by coupling a practical
50 DNAPL dissolution model with uncertainty quantification methods. Simulations of flow-cell
51 experiments demonstrated the worth of DNAPL delineation for constraining source zone
52 dissipation uncertainties, estimated a priori through parameterization of DNAPL distributions. In
53 turn, parameterizing system heterogeneities in greater detail was necessary to estimate unbiased
54 source zone characteristics and lifespans, derived from the assimilation of complex DNAPL
55 dissolution trends observed in monitoring profiles. Our results demonstrated how available site
56 data can be integrated into a decision-support modeling framework to inform data collection
57 strategies and remedial designs.

58

59 **Index Terms and Keywords**

60

61 Source zone persistence, source zone heterogeneity, DNAPL dissolution rates, conceptual
62 assumptions, data assimilation, model parameterization, remedial-decision making, practical
63 recommendations

64

65 **1. Introduction**

66

67 Mathematical modeling can provide valuable insights for decision support at hazardous waste sites
68 with groundwater impacted by dense non-aqueous phase liquids (DNAPLs). However, a gap
69 between simplistic analytical screening models and overly complex numerical simulators has
70 limited their applicability for estimating DNAPL longevity and dissolution rates. Researchers have
71 focused on estimating distributions of DNAPL saturation, referred to as the source zone
72 architecture, or DNAPL dissolution rates from synthetically-generated datasets using several
73 mathematical approaches to simulating mass transfer. Several studies considered either a local
74 equilibrium assumption (LEA) or Gilland-Sherwood models of interphase mass transfer (Kang et
75 al. 2021a; Powers et al., 1992, 1994; Saenton & Illangasekare, 2004).

76

77 Decision-support modeling incorporating LEA is questionable because heterogeneity of aquifer
78 hydraulic properties and source architecture can induce flow bypassing and mass transfer rate
79 limitations, resulting in nonequilibrium concentrations typically observed at field sites (Falta,
80 2003; Kokkinaki et al., 2013). Similarly, Gilland-Sherwood models rely on correlations between
81 empirical coefficients and soil particle sizes that were determined under specific bench-scale
82 conditions, which may not be applicable to field-scale problems with different hydraulic properties
83 (Powers et al., 1992; Saenton & Illangasekare, 2007). Moreover, the computational cost of pore-
84 scale numerical models incorporating LEA and Gilland-Sherwood correlations limits their
85 practicality for data assimilation and uncertainty quantification (Falta, 2003; Kokkinaki et al.,
86 2013; Powers et al., 1994). An alternative method is predicated on a lumped-process, scale-
87 dependent mass transfer coefficient estimated from monitoring data (Guo et al., 2020; Mobile et
88 al., 2012; Park & Parker, 2005). However, estimating mass transfer rates exclusively from

89 historical monitoring may bias predictions of source longevity because of architectural changes.
90 For example, early in the life cycle of a DNAPL source zone, the contributions of slowly dissolving
91 pools governing complete depletion may not be discernible in discharge data (Abriola et al., 2013).

92
93 Multistage DNAPL dissolution, typically observed at contaminated sites and in dissolution
94 experiments, arises from heterogeneity of source zone architecture (Figure 1) primarily comprised
95 by residual ganglia and high-saturation DNAPL pools (Christ et al., 2010; Dekker & Abriola,
96 2000; DiFilippo & Brusseau, 2008; Lemke & Abriola, 2006; Parker & Park, 2004). Consequently,
97 a number of high-resolution site characterization (HRSC) technologies have been developed
98 (Einarson et al., 2018; Horst et al., 2018; Kueper et al., 2014). Delineation of DNAPLs comprised
99 by chlorinated ethenes is possible with dye-enhanced laser induced fluorescence (DyeLIF) and
100 confirmatory sampling, and with indirect observation methods, such as multilevel monitoring and
101 groundwater extraction systems, passive flux meters, push-pull tracer tests, etc. (Horst et al. 2018;
102 Huang et al. 2010; ITRC, 2010; Kueper et al., 2014). Although HRSC may help constrain DNAPL
103 distribution, quantifying residual mass and saturation directly is not possible (Einarson et al.,
104 2018). Thus, inverse modeling techniques have been applied to quantify lumped-process mass
105 transfer coefficients from monitoring data Marble et al., 2008; Mobile et al., 2012; Saenton &
106 Illangasekare, 2004), or to estimate source zone architectures from borehole and geophysical
107 measurements using physically-based parameterization mechanisms (Kang et al. 2021a, 2021b).
108 Kang et al. (2022) demonstrated a novel Bayesian inversion framework to reconstruct complex
109 permeability and DNAPL saturation fields, subsequently parameterizing an upscaled model of
110 DNAPL dissolution to reproduce experimental source depletion trends.

111
112 Upscaled (domain-averaged) models lacking a physical mass transfer basis cannot assimilate
113 HRSC data and have proved ineffective at explaining and predicting DNAPL dissolution behavior
114 (Christ et al., 2006; Kokkinaki et al., 2014; Marble et al., 2008). However, upscaled models
115 incorporating metrics describing the source zone architecture, such as the ganglia-to-pool (GTP)
116 mass ratio, have shown improved success (Abriola et al. 2013; Christ et al., 2010; DiFilippo &
117 Brusseau, 2011). Stewart et al. (2021) developed a volume-averaged (VA) model of DNAPL
118 dissolution predicated on characteristic length scales of DNAPL accumulations and their relative
119 location along groundwater flow paths, explicitly accounting for mass transfer processes at the
120 source zone scale (Figure 1). The model accurately reproduced complex DNAPL dissolution
121 observed in laboratory, numerical, and field experiments by parameterizing initial, and estimable
122 system characteristics without undertaking history-matching. The VA model is therefore able to
123 assimilate HRSC and/or monitoring data to estimate source dissipation timeframes with
124 computational efficiency in a scalable and physically-based manner. Such capabilities make the
125 VA model suitable for evaluating site conceptual assumptions and quantifying uncertainties, which
126 is necessary for effective remedial-decision support (Abriola, 2005).

127
128 The primary objectives in this work were to (i) identify the relative contribution of VA mass
129 transfer parameters to source zone dissipation uncertainties, and (ii) investigate how model
130 parameterization influences predictive bias through monitoring data assimilation. The VA DNAPL
131 dissolution model developed by Stewart et al. (2021) was coupled with sensitivity and uncertainty
132 analysis methods to evaluate the worth of direct and indirect source zone measurements for
133 constraining system parameters and model uncertainty. High-resolution datasets of two DNAPL
134 dissolution experiments were leveraged to evaluate data-driven conceptual assumptions on

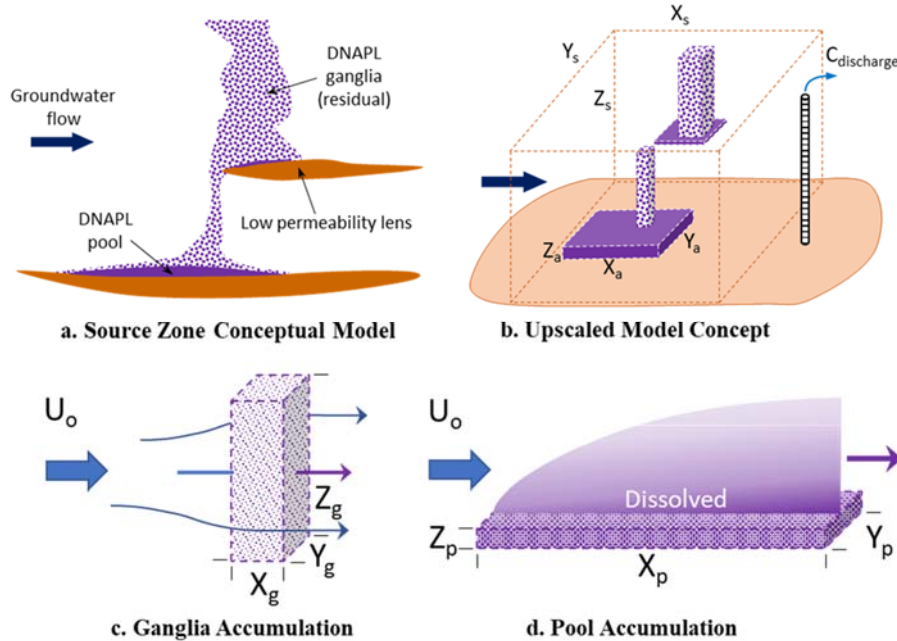
135 modeling outcomes. Our findings elucidate on model design to quantify unbiased DNAPL
 136 persistence uncertainties, yielding recommendations on HRSC and monitoring data assimilation
 137 for constraining future source zone behavior.

138 2. Upscaled and Volume-Averaged Model of DNAPL Dissolution

139
 140 Volume-averaging relaxes the need to specify precise locations of DNAPL accumulations within
 141 a finely discretized domain. The approach facilitates the incorporation of physically-based mass
 142 transfer relationships for complex field-scale dissolution behavior with computational efficiency.
 143 As presented by Stewart et al. (2021), dissolution of a single DNAPL accumulation, defined as a
 144 volume of relative uniformity in saturation, can be simulated by a generalized upscaled mass
 145 transfer function:

$$k_a = \frac{U_0}{V_s} \left[A_{a,yz} k_r(m_a) + A_{a,xy} \sqrt{\frac{4\alpha_T}{\pi X_a}} \left(\frac{m_a}{m_{a,0}} \right)^\gamma \right] \quad (1)$$

147



148
 149 **Figure 1.** Conceptual and volume-averaged model representations (a and b, respectively) of a DNAPL source zone
 150 comprised by characteristic accumulations of (c) residual ganglia and (d) pools. Adapted from Stewart et al. (2021).
 151

152 Where interphase mass transfer (k_a^N) from an individual DNAPL accumulation “a” is driven by
 153 the local Darcy groundwater velocity (U_0) upscaled by a source zone reference volume (V_s)
 154 encompassing the DNAPL masses. The term on the left inside the brackets represents dissolution
 155 attributable to through flow (Figure 1c), which is proportional to the projected area facing flow
 156 ($A_{a,yz} = Y_a Z_a$) of “a”. Flow through “a” is regulated by the soil relative permeability (k_r) which
 157 gradually increases the DNAPL dissolution rate as the DNAPL volume is reduced. The term on
 158 the right represents dissolution attributable to dispersion into bypassing flow (Figure 1d), which is
 159 proportional to the hydrodynamic transverse dispersivity (α_T) around “a” and the horizontal area
 160 of the accumulation ($A_{a,xy} = X_a Y_a$). Mass dissolution from low DNAPL saturations, i.e., ganglia,

161 are dominated by flow through, while high saturation zones, i.e., pools, can be dominated by
 162 dispersion. The normalized mass (m/m_0) term reflects a transient reduction of DNAPL interfacial
 163 area. Theoretically, the dimensionless exponent $\gamma = 2/3$ for ganglia-dominated accumulations, and
 164 $\gamma = 1/2$ for pool-dominated accumulations. The γ exponent may be adjusted during model history-
 165 matching to allow for deviations from conceptual mass transfer assumptions but is expected to fall
 166 within this relatively narrow range (Stewart et al., 2021).

167

168 **2.1. Simulation of DNAPL Dissolution Experiments**

169

170 Flow-cell experiments presented by DiFilippo et al. (2010) and analyzed by Guo et al. (2020) with
 171 a simplified inverse modeling method were utilized in this study. Stewart et al. (2021) simulated
 172 these experiments with the VA approach by explicitly accounting for DNAPL saturation
 173 distributions, flow field characteristics, and soil properties. The dissolution experiments consisted
 174 of two source zone scenarios: a “mixed” DNAPL architecture comprised by a ganglia-dominated
 175 accumulation and a pool-dominated accumulation in homogeneous sand, and multiple DNAPL
 176 accumulations in a “heterogeneous” soil. Details of model conceptualization and simulation results
 177 were presented in Stewart et al. (2021).

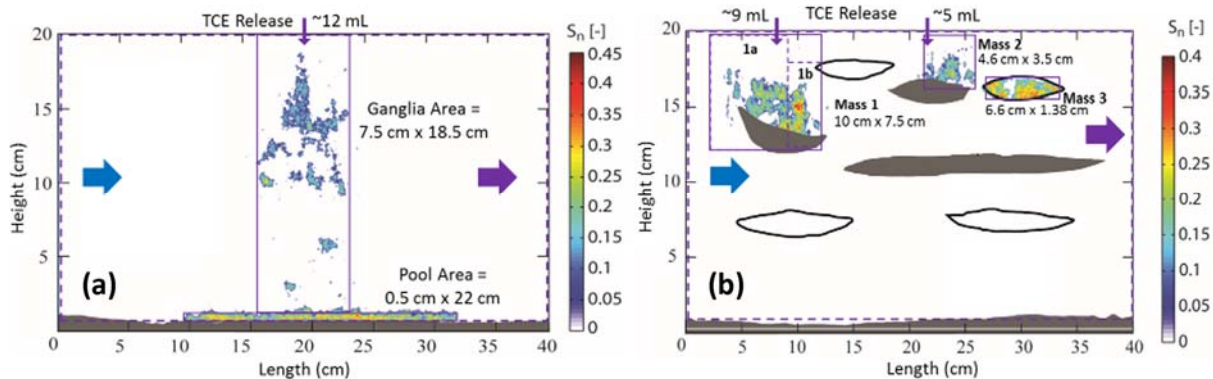
178

179 *2.1.1. Mixed DNAPL Architecture*

180

181 The “mixed” source zone experiment conducted by DiFilippo et al. (2010) consisted of a uniform
 182 pack of sand (40/50 mesh) with a 2-cm thick capillary barrier located along the bottom of the test
 183 cell (Figure 2a). An injection of ~12 milliliters of trichloroethene (TCE) at the top of the test cell
 184 followed by 48-hour period prior to flow initiation generated a stable source zone architecture
 185 consisting of a vertical ganglia zone underlain by a pool. The DNAPL saturation distribution was
 186 characterized using a light reflection visualization (LRV) method and TCE effluent concentrations
 187 were monitored until source zone depletion.

188



189 **Figure 2.** Model conceptualizations of the flow-cell experiments: (a) mixed source zone architecture and (b)
 190 heterogeneous source zone. Sub-volumes (purple rectangles) correspond to DNAPL accumulations with distinct
 191 saturations encompassed by the source volume (purple dashed line). Adapted from Stewart et al. (2021).

192

193 *2.1.2. Multiple DNAPL accumulations in Heterogeneous Soil*

194

195 The test cell of the heterogeneous source experiment (Figure 2b) consisted of a matrix of
 196 homogeneous sand (40/50 mesh) with coarser (20/30 mesh) and finer (70/100 mesh) lenticular
 197

198 zones (DeFilippo et al., 2010; Guo et al., 2020). An injection of ~15 milliliters of TCE at the top
 199 of the cell was distributed between two ports with 66% in the far left (upgradient) port and 33% in
 200 the center (downgradient) port (DeFilippo et al. 2010). The central release generated two distinct
 201 accumulations: one above a fine-grained lens and one within a coarse-grained lens. The coarse
 202 lens had an intrinsic permeability approximately 3.5 times higher than the surrounding bulk sands
 203 (DeFilippo et al., 2010), resulting in a higher velocity through this material than in the surrounding
 204 matrix. As shown in Figure 2b, Stewart et al. (2021) subdivided the upgradient accumulation into
 205 two accumulations on the basis of characteristic saturations to accurately capture the measured
 206 TCE effluent breakthrough. Sequential dissolution inhibition was also implemented by Stewart et
 207 al. (2021) for the two downgradient accumulations on the basis of their relative locations along the
 208 flow path. Nomenclature for variables in the model are presented in Table 1.

209
210 **Table 1.** Nomenclature of input parameters used in the VA model of the flow-cell experiments.

Parameter	Mixed Source		Heterogeneous Source				Unit
Mass	<i>Mass G.</i>	<i>Mass P.</i>	<i>Mass 1A</i>	<i>Mass 1B</i>	<i>Mass 2</i>	<i>Mass 3</i>	g
Length	X_g	X_p	X_{1A}	X_{1B}	X_2	X_3	m
Width	Y_g	Y_p	Y_{1A}	Y_{1B}	Y_2	Y_3	m
Height	Z_g	Z_p	Z_{1A}	Z_{1B}	Z_2	Z_3	m
NAPL Saturation	S_g^N	S_p^N	S_{1A}^N	S_{1B}^N	S_2^N	S_3^N	%
Area Facing Flow	YZ_g	YZ_p	YZ_{1A}	YZ_{1B}	YZ_2	YZ_3	m ²
Dispersive Area	XY_g	XY_p	XY_{1A}	XY_{1B}	XY_2	XY_3	m ²
Dispersivity	$\alpha_{T,g}$	$\alpha_{T,p}$	$\alpha_{T,1A}$	$\alpha_{T,1B}$	$\alpha_{T,2}$	$\alpha_{T,3}$	m
γ	γ^g	γ^p	γ^{1A}	γ^{1B}	γ^2	γ^3	-

211
212 **2.2. Sensitivity Analysis**
213
214 Model output variability was evaluated with local sensitivity analysis by systematically perturbing
215 input parameters around reference values conceptualized in Stewart et al. (2021). The goal was to
216 compare relative sensitivities with respect to measured discharge concentrations and with respect
217 to the time required to reach cleanup concentrations, defined here as time of remediation (TOR).
218 Both metrics were evaluated using the same model input variability around base parameter sets.
219 Because the plausible variability range of some parameters and their corresponding outputs differs
220 by orders of magnitude compared to those of other parameters, sensitivity coefficients were scaled
221 by maximum values to provide a relative comparison metric of simulation error. All sensitivity
222 analyses were automated coupling SENSAN and PEST software (Watermark Numerical
223 Computing, 2018) for calculation fidelity.

224
225 *2.2.1. Sensitivities with respect to TCE discharge concentrations*
226

227 Normalized sensitivity coefficients (X_{TCE}) were calculated on the basis of root mean squared errors
228 (RMSE) between simulated (sim_i) and measured (obs_i) discharge concentrations as:

$$X_{TCE} = \left(\frac{|\partial RMSE| / RMSE(a)}{|\Delta a / a|} \right) / X_{TCE}^{max} \quad (2)$$

230
231 where:

232

$$RMSE = \left[\frac{1}{N} \sum_{i=1}^N (sim_i - obs_i)^2 \right]^{1/2} \quad (3)$$

233

$$\partial RMSE = RMSE(\Delta a) - RMSE(a) \quad (4)$$

234

235 a = base parameter; Δa = perturbed parameter – a ; N = number of TCE effluent measurements. All
 236 sensitivity coefficients were normalized by maximum values (X_{TCE}^{max}) to provide a relative
 237 comparison metric of model sensitivities.

238

239 2.2.2. Sensitivities with respect to TOR

240

241 Provided with a cleanup concentration input, the VA model calculates the time required to reach
 242 the target value (e.g., contaminant MCL). Using the base parameter sets, which reflect detailed
 243 experimental conditions and initial source zone properties, TOR was calculated for both
 244 experiments setting target concentrations at $C = 0.005$ mg/L. Sensitivity coefficients normalized
 245 by maximum values (X_{TOR}^{max}) were calculated as:

246

$$X_{TOR} = \left(\frac{RMSE(\Delta a)}{|\Delta a / a|} \right) / X_{TOR}^{max} \quad (5)$$

247 3. Uncertainty Analysis

248

249 Source zone metrics controlling field-scale dissolution include DNAPL mass and distribution
 250 (Abriola et al., 2013). Uncertainties associated to both metrics can therefore propagate to model
 251 predictive uncertainties (Abriola, 2005; Tang, 2019). Prior (pre-history matching) parameter and
 252 predictive uncertainties can be informed by expert knowledge and/or by site characterization (e.g.,
 253 DNAPL delineation, projected flow through area), whereas posterior (post-history matching)
 254 uncertainties may be reduced and quantified through history-matching of monitoring data.
 255 Because volume-averaging eliminates spatial parameter correlations, the prior uncertainty of mass
 256 transfer parameters was expressed through statistically uncorrelated uncertainty bounds (archived
 257 data file). All initial (mean) parameter values were inherited from Stewart et al. (2021).

258

259 Uncertainty bounds of characteristic dimensions (V_a) and mass (m_a) of DNAPL accumulations
 260 were designed so that $1\% < S_a^N < 60\%$ and $\sum V_a < V_S$ in both experiments; where DNAPL saturation
 261 (S_a^N) of the pore space (ϕ) is also a function of DNAPL density (ρ_n) as indicated by Equation 6.
 262 Per sensitivity results, upscaling parameters (V_S , U_0 , and ϕ) were assumed well constrained by the
 263 monitoring scale and removed from predictive uncertainty evaluations. Uncertainty analyses were
 264 focused on m_a , V_a , α_T , and γ pertaining to each DNAPL accumulation. Linear and nonlinear
 265 uncertainty quantification methods were implemented to understand drivers of model uncertainties
 266 and bias emerging from data-driven conceptual assumptions.

267

$$S_a^N = \frac{m_a}{V_a \phi \rho_n} \quad (6)$$

268

269 **3.1. Linear Analysis Methods**

270

271 Model linearization expressed in Equation 7 is the primary assumption in first-order second-
 272 moment (FOSM) analysis (Doherty, 2015). Equation 7 indicates that a vector of measurements of
 273 system state \mathbf{h} equals the action of the model \mathbf{Z} on a vector of parameters \mathbf{k} plus a vector of
 274 measurement noise $\boldsymbol{\varepsilon}$. Prior model uncertainty was expressed by Equation 8 assuming a multi-
 275 gaussian probability density function (PDF), defined by mean parameter values $\underline{\mathbf{k}}$ and a diagonal
 276 covariance matrix $\mathbf{C}(\mathbf{k})$. Likewise, FOSM analysis assumes a multi-gaussian PDF of $\boldsymbol{\varepsilon}$ (Equation
 277 9), defined by mean values of zero and a diagonal covariance matrix $\mathbf{C}(\boldsymbol{\varepsilon})$. Jacobian matrices \mathbf{Z}
 278 were weighted by the inverse of the standard deviation (σ) of $\boldsymbol{\varepsilon}$. The misfit between simulated
 279 (Stewart et al., 2021) and measured TCE concentrations was used to define $\boldsymbol{\varepsilon}$, where $\sigma_{\boldsymbol{\varepsilon}}^{-1}$ values
 280 were calculated with the PEST-based utility PWTADJ2 (Watermark Numerical Computing, 2018)
 281 as observations weights for FOSM analyses.

282

$$\mathbf{h} = \mathbf{Z}\mathbf{k} + \boldsymbol{\varepsilon} \quad (7)$$

283

$$\mathbf{k} \sim \mathbf{N}[\underline{\mathbf{k}}, \mathbf{C}(\mathbf{k})] \quad (8)$$

284

$$\boldsymbol{\varepsilon} \sim \mathbf{N}[\mathbf{0}, \mathbf{C}(\boldsymbol{\varepsilon})] \quad (9)$$

285

$$s = \mathbf{y}^t\mathbf{k} \quad (10)$$

286

$$\sigma_s^2 = \mathbf{y}^t\mathbf{C}(\mathbf{k})\mathbf{y} \quad (11)$$

287

$$\mathbf{C}'(\mathbf{k}) = \mathbf{C}(\mathbf{k}) - \mathbf{C}(\mathbf{k})\mathbf{Z}^t[\mathbf{Z}\mathbf{C}(\mathbf{k})\mathbf{Z}^t + \mathbf{C}(\boldsymbol{\varepsilon})]^{-1}\mathbf{Z}\mathbf{C}(\mathbf{k}) \quad (12)$$

288

$$\sigma'_s{}^2 = \mathbf{y}^t\mathbf{C}'(\mathbf{k})\mathbf{y} \quad (13)$$

289

290 Linearization of a model prediction s (Equation 10) depends on a vector of sensitivities of s (TOR)
 291 with respect to \mathbf{k} , where the prior variance of s (Equation 11) is obtained through covariance
 292 propagation (Doherty, 2015). The posterior parameter covariance matrix (Equation 12), obtained
 293 by history-matching conditioning, was used to estimate posterior TOR uncertainty variance
 294 (Equation 13). All parameters were log-transformed to reduce their nonlinearity with respect to
 295 model outputs. Linear analyses were performed with the utility programs GENLINPRED and
 296 PREDUNC (Watermark Numerical Computing, 2018) to understand how TCE monitoring profiles
 297 constrain source zone properties, and thereby, TOR uncertainties.

298

299 *3.1.1. Relative parameter uncertainty variance (RUVR) reduction*

300

301 This statistical metric was used to evaluate the ability of dissolved TCE concentrations to reduce
 302 the prior uncertainty variance (σ_i^2) of each parameter (i) encapsulated in $\mathbf{C}(\mathbf{k})$. Equation 14 defines
 303 this metric upon extracting posterior parameter uncertainty variances ($\sigma'_i{}^2$) from $\mathbf{C}'(\mathbf{k})$ as:

304

$$RUVR_i = 1 - \frac{\sigma'_i{}^2}{\sigma_i^2} \quad (14)$$

305

306 3.1.2. Prior and posterior parameter contributions to predictive uncertainty

307
308 The contribution of an individual parameter to the uncertainty of a prediction is defined as the fall
309 of predictive uncertainty resulting from acquiring perfect knowledge of the parameter (Doherty,
310 2015). Hence, individual parameters were systematically removed from FOSM calculations to
311 investigate their relative contributions to TOR uncertainty. Because history-matching information
312 may be shared between several model parameters, the posterior contribution of a parameter could
313 increase in relation to its prior contribution, indicating a correlation with another parameter
314 (Doherty, 2015). While sensitivity analyses were useful to examine relative model error incurred
315 by perturbing individual parameters, considering parameter correlations for TOR uncertainty
316 estimation allowed assessing the worth of HRSC over history-matching for constraining the
317 models.

318 319 3.1.3. Data-Worth Analysis

320
321 The ability of spatial or temporal data to reduce the uncertainty of model predictions defines its
322 worth (Doherty & Moore, 2020; Finsterle, 2005). The worth of individual measurements of TCE
323 concentrations was quantified to understand how monitoring profiles reduce TOR uncertainty.
324 Data-worth analyses were also tied to parameter RUVR, further elucidating upon the additional
325 benefit of HRSC for constraining remaining model uncertainties.

326

327 3.2. Nonlinear Analysis Methods

328
329 Posterior TOR uncertainties were quantified using the iterative ensemble smoother PESTPP-iES
330 (White et al., 2020). Multi-gaussian prior parameter PDFs were defined by uncertainty bounds
331 spanning $\pm 2\sigma$ from initial (mean = μ) values, representing 95% confidence intervals. PESTPP-
332 iES undertakes Monte-Carlo sampling of parameter uncertainty bounds generating model
333 realizations (ensembles) which are upgraded with the Gauss-Levenberg-Marquardt (GLM)
334 optimization algorithm. Rather than simply fitting simulation results to data, PESTPP-iES can
335 generate observation ensembles considering multi-gaussian PDFs of ε (White, 2018). Here, all
336 experimental TCE concentrations were assigned an observation weight value of 1 with $\sigma_\varepsilon = 10$
337 mg/L, to simultaneously estimate model parameters and quantify the nonlinear uncertainty of TOR
338 in a stochastic manner. This approach was implemented to evaluate TOR uncertainties and bias
339 arising from source zone conceptual assumptions driven by data availability.

340
341 In practice, HRSC data may help constrain source zone architecture, and thereby model
342 conceptualizations. However, high predictive uncertainties may remain because of the inability to
343 directly measure DNAPL mass and S_a^N . The benefit of data assimilation for constraining model
344 uncertainties was investigated by estimating m_a , V_a , $\alpha_{T,a}$, and γ^a parameters in both experiments
345 from partial and complete monitoring profiles. The resulting source dissipation timeframes were
346 referred to as Posterior A (~13 days of monitoring), Posterior B (20 days) and Posterior All (26
347 days). Additionally, the heterogeneous experiment was conceptualized with 2 (2M), 3 (3M) and 4
348 (4M) DNAPL accumulations to examine TOR uncertainty and bias induced by history-matching
349 of the entire TCE monitoring profile. The 2M model included “mass 1” and lumped “mass 2” and
350 “mass 3” into a single accumulation (2M-3) based on the two release points, while the 3M model
351 included those 3 distinct DNAPL accumulations. The 4M model subdivided “mass 1” into 1A and

352 1B (Figure 2b). Except for the 2M Model, the 3M and 4M models included an enhanced dissolution
353 parameter to represent flow channelization through the coarse lens in which “mass 3” was
354 embedded. Following a variability range reported in the literature (Klenk & Grathwohl, 2002), the
355 prior uncertainty bounds of α_T parameters were defined as $5e^{-4} < \alpha_T \text{ (m)} < 2e^{-3}$ in both experiments,
356 except for $0 (1e^{-15}) < \alpha_{T,3} \text{ (m)} < 0.002$ in the coarse sand lens of the heterogeneous experiment,
357 where $\alpha_{T,3} = 0$ m provided the best match to measured TCE concentrations (Stewart et al., 2021).

358 4. Results and Discussion

359

360 4.1. Sensitivity Analysis

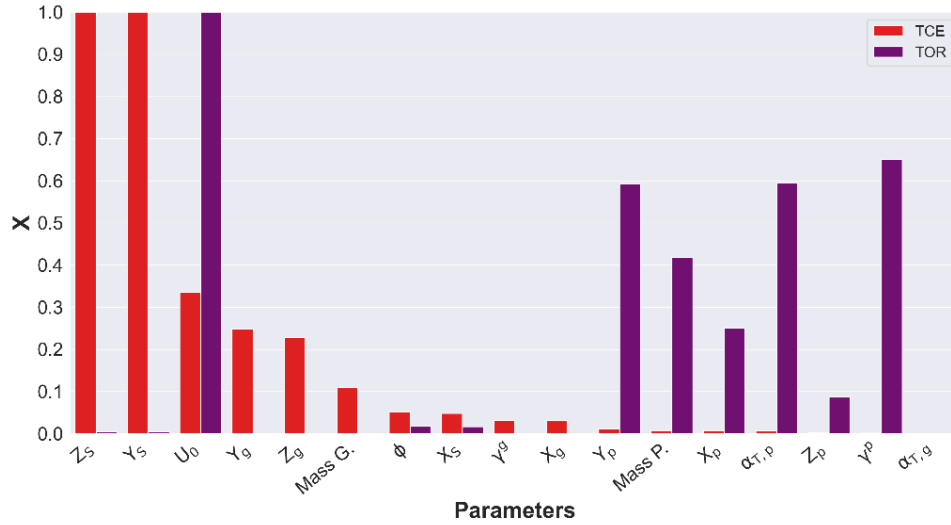
361

362 As shown in Figures 3 and 4, the greatest model sensitivities with respect to matching TCE
363 concentrations (X_{TCE}) corresponded to the source zone area (Z_S and Y_S) orthogonal to the flow
364 direction and groundwater velocity (U_θ). The former accounts for any dilution in the monitoring
365 scale, while the latter had a prominent impact on TOR in both experiments. The role of V_S and U_θ
366 on scaling mass transfer processes emphasized the need to constrain them by the monitoring scale
367 to avoid model errors induced by data assimilation. Figure 3 also indicated that the projected area
368 facing flow (YZ_g) of the ganglia-dominated accumulation, rather than γ^g or ganglia mass, was
369 responsible for peak aqueous-phase concentrations. Similarly, Figure 4 shows the projected area
370 YZ_{1A} of the most upgradient, low-saturation accumulation 1A in a high-ranked position. These
371 X_{TCE} results suggested that S_a^N parameters (V_a and $Mass$) of ganglia-dominated accumulations
372 responsible for peak concentrations do not impact TOR when a pool-dominated accumulation is
373 also present; yet their estimation via history-matching may be valuable for remedial designs.
374 Conversely, sensitivity with respect to TOR (X_{TOR}) was dominated by DNAPL pool saturation
375 (S_p^N) parameters, transverse dispersivity ($\alpha_{T,p}$), and depletion exponent (γ^p). The negligible X_{TCE}
376 values of pool parameters suggested difficulty in estimating them from monitoring data alone and
377 value in HRSC for refining characteristic parameters of the pool.

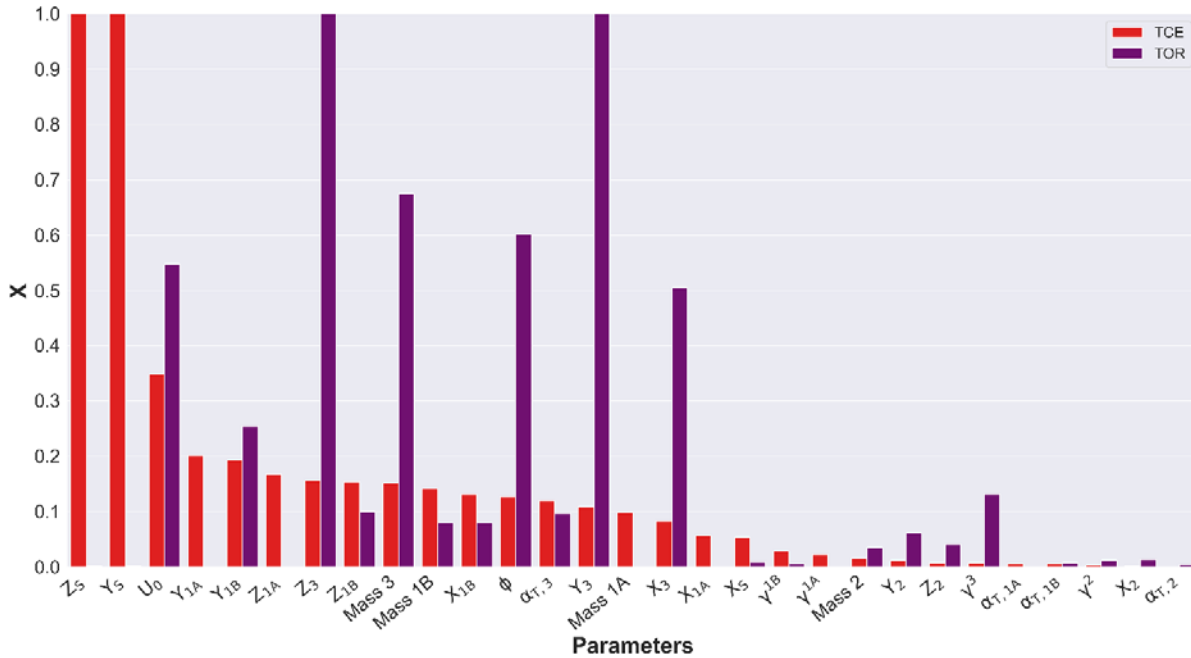
378

379 In contrast to negligible X_{TCE} values by pool parameters in the mixed experiment (Figure 3), X_{TCE}
380 rankings of S_3^N parameters in the heterogeneous experiment (Figure 4) suggested that high-
381 saturation DNAPL accumulations may not exclusively reflect pool fractions of source zones.
382 Typically, the small cross-sectional areas available for dissolution by groundwater flow through
383 DNAPL pools reduces their relative contribution to mass flux, compared to ganglia-dominated
384 accumulations. However, as indicated in Figure 4, the morphology of DNAPL accumulation 3,
385 controlled by flow-field heterogeneity, influenced both X_{TCE} and X_{TOR} rankings in the
386 heterogeneous experiment. The predictive advantage of generalizing mass transfer processes
387 irrespective of S_a^N (Equation 1) over upscaled models predicated on the GTP mass ratio, was
388 further evidenced by a similar effect on X_{TCE} and X_{TOR} incurred by perturbing $\alpha_{T,3}$ (Figure 4).
389 Conversely, the variability of other α_T parameters in both experiments only influenced X_{TOR} .

390



391 **Figure 3.** Sensitivity coefficients with respect to source discharge concentrations measured in the “mixed
 392 architecture” experiment and with respect to the simulated TOR.
 393
 394



395 **Figure 4.** Sensitivity coefficients with respect to source discharge concentrations measured in the “heterogeneous
 396 architecture” experiment and with respect to the simulated TOR.
 397
 398

399 **4.2. Linear Analysis**

400
 401 Prior (σ_{TOR}) and posterior (σ'_{TOR}) standard deviations of TOR uncertainty estimated with FOSM
 402 analysis and mean (μ_{TOR}) values for both experiments are presented in Table 2. Results shown
 403 were calculated using the complete TCE monitoring profiles. As indicated, history-matching
 404 significantly constrained prior TOR uncertainties despite low X_{TCE} values of TOR-sensitive
 405 parameters pertaining to high- S_a^N accumulations.
 406

407

Table 2. Predictive uncertainty of mixed and heterogeneous experiments.

Experiment	μ_{TOR} (days)	σ_{TOR} (days)	σ'_{TOR} (days)
Mixed	27.9	19.8	8.6
Heterogeneous	28.6	20.5	1.7

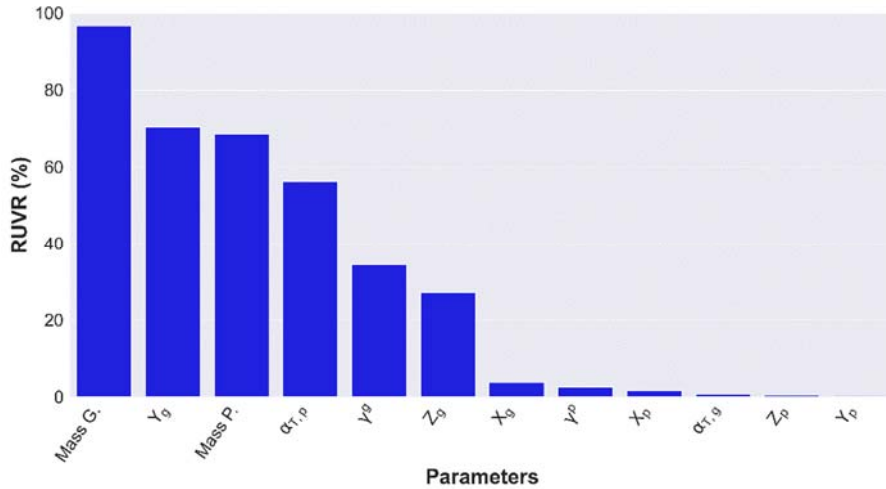
408

409 *4.2.1. Relative Parameter Uncertainty Variance Reduction*

410

411 Figures 5 and 6 show the benefit of history-matching for reducing prior parameter uncertainties.
 412 Despite negligible X_{TCE} values corresponding to the pool mass and $\alpha_{T,p}$ of the mixed experiment
 413 (Figure 3), history-matching reduced the prior uncertainty of these parameters by $\sim 70\%$ and $\sim 60\%$,
 414 respectively (Figure 5). The low uncertainty reduction of γ^p (Figure 5), to which TOR was sensitive
 415 (Figure 3), demonstrated the benefit of coupling upscaled modeling with stochastic analysis tools
 416 for predicting DNAPL longevity timeframes when mass transfer parameters remain unconstrained.
 417 In turn, sensitivity and FOSM analyses of the mixed experiment coincided in a low-ranked $\alpha_{T,g}$,
 418 suggesting that its prior (default) value of 0.001 m is reasonable for simulating dissolution of
 419 ganglia-dominated accumulations.

420



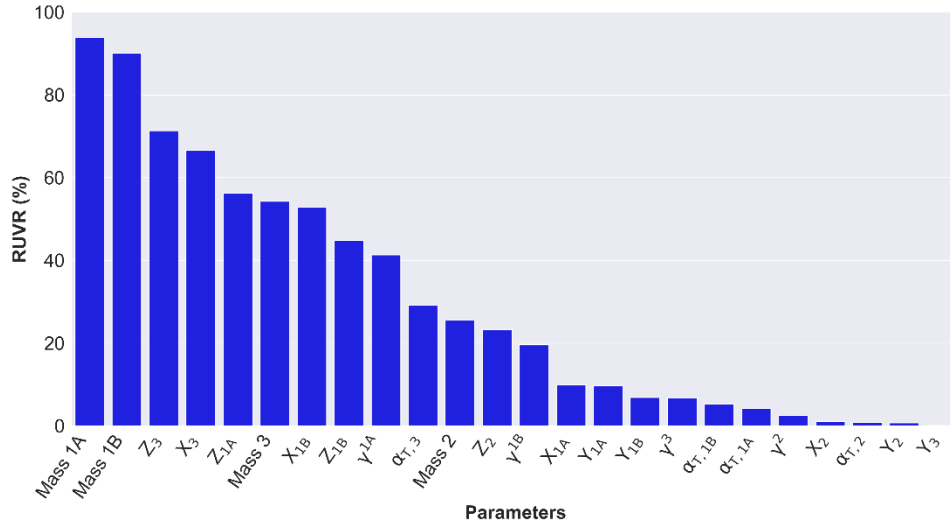
421

422 **Figure 5.** Relative uncertainty variance reduction of VA model parameters of mixed experiment.

423

424 Difficulties in reducing prior uncertainty of the γ parameters in the heterogeneous experiment are
 425 reflected in Figure 6. Yet the prior uncertainty of S_a^N parameters of DNAPL accumulations 1A
 426 (S_{1A}^N), 1B (S_{1B}^N), and 3 (S_3^N) was reduced by approximately more than 50%. The higher RUVR of
 427 S_3^N with respect to other S_a^N parameters was attributed to the sequential dissolution of upgradient
 428 DNAPL masses, allowing the tailing segment of the TCE monitoring profile to constrain the
 429 remaining source architecture (S_3^N). These results implied that modeling efforts supporting the
 430 characterization of sites with aged, pool-dominated source zones, may benefit from history-
 431 matching of monitoring profiles. However, situations with scarce monitoring data and significant
 432 uncertainties on S_a^N distributions along groundwater flow paths may warrant HRSC efforts. In
 433 turn, source characterization data such as DyeLIF and Hydraulic Profiling Tool (HPT) (Horst et
 434 al., 2018) can be leveraged for VA model parameterization, while FOSM analyses can help guide
 435 additional data collection efforts to constrain DNAPL dissolution trends.

436



437 **Figure 6.** Relative uncertainty variance reduction of VA model parameters of heterogeneous experiment.
 438
 439

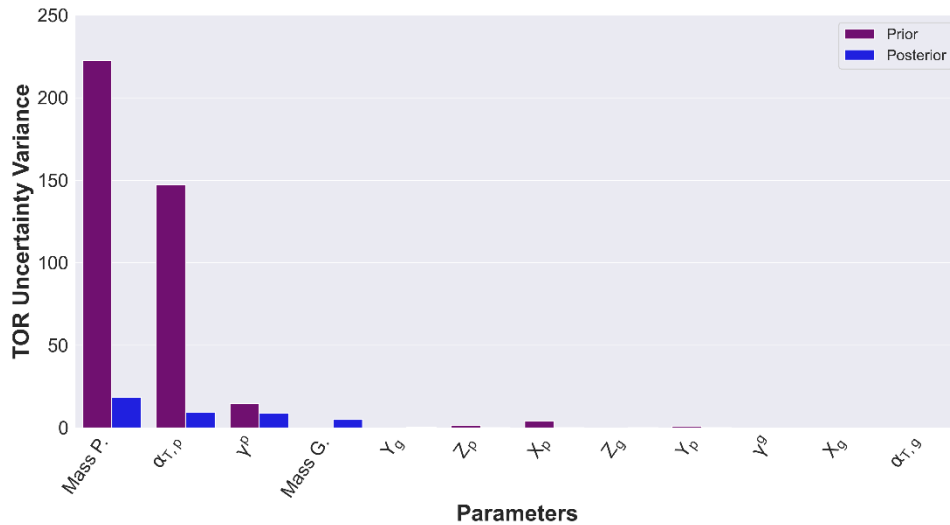
440 *4.2.2. Prior and posterior parameter contributions to predictive uncertainty*
 441

442 As shown in Figure 7, FOSM analyses validated negligible X_{TOR} values caused by the ganglia
 443 parameters in the mixed experiment. Although the pool dispersive area (YX_p) and γ^p influenced
 444 X_{TOR} results (Figure 3), prior and posterior TOR uncertainties of the mixed experiment were clearly
 445 driven by the pool mass and $\alpha_{T,p}$ (Figure 7). Likewise, Figure 8 indicated that the primary drivers
 446 of prior TOR uncertainty in the heterogenous experiment were S_3^N , $\alpha_{T,3}$, and γ^3 . Repeating FOSM
 447 calculations with uncertainty bounds defined as $0 < \alpha_T$ (m) < 0.01 for all DNAPL accumulations
 448 in the heterogeneous experiment did not alter the uncertainty rankings shown in Figure 8. Results
 449 of both experiments agreed on the significance of dispersive mass transfer (α_T) from high-
 450 saturation DNAPL accumulations in regulating TOR. However, the accurate replication of the
 451 heterogenous source dissolution trend with $\alpha_{T,3} = 0$ m was attributed to the contrast in grain sizes,
 452 limiting dispersion from the coarse-grained lenticular zone into the finer surrounding sands despite
 453 high $S_{3,0^N}$ values.
 454

455 Unlike the empirical mass depletion exponent γ^3 , α_T may be directly measured at contaminated
 456 sites to directly constrain mass transfer uncertainties. Examples of field methods include push-pull
 457 tracer tests, borehole and HPT logging, and discrete groundwater sampling with direct push
 458 technology (DPT). These data may be interpreted with 2D analytical modeling (Huang et al.,
 459 2010), grain-size correlations with soil hydraulic conductivity and α_T (Carey et al., 2018), and
 460 spatial moment analysis (Rockhold et al., 2016), respectively. Nonetheless, the α_T component of
 461 DNAPL dissolution expressed in Equation 1 should not be confused with plume-scale
 462 macrodispersion. While dispersivity at the source-zone and plume scales is driven by mechanical
 463 or hydrodynamic mixing along tortuous flow paths (Molz, 2015), coupling a VA model of DNAPL
 464 dissolution with a downgradient contaminant plume model may require two different α_T values
 465 based upon site-specific conditions. Several studies have demonstrated the relationship between
 466 soil grain size and α_T (Carey et al., 2018), concurring with its role on DNAPL mass transfer
 467 (Figures 7 and 8). This is in contrast to Gilland-Sherwood mass transfer correlations which rely
 468 upon aqueous-phase transport models for the contribution of α_T to DNAPL dissolution (Yang et
 469 al., 2019).

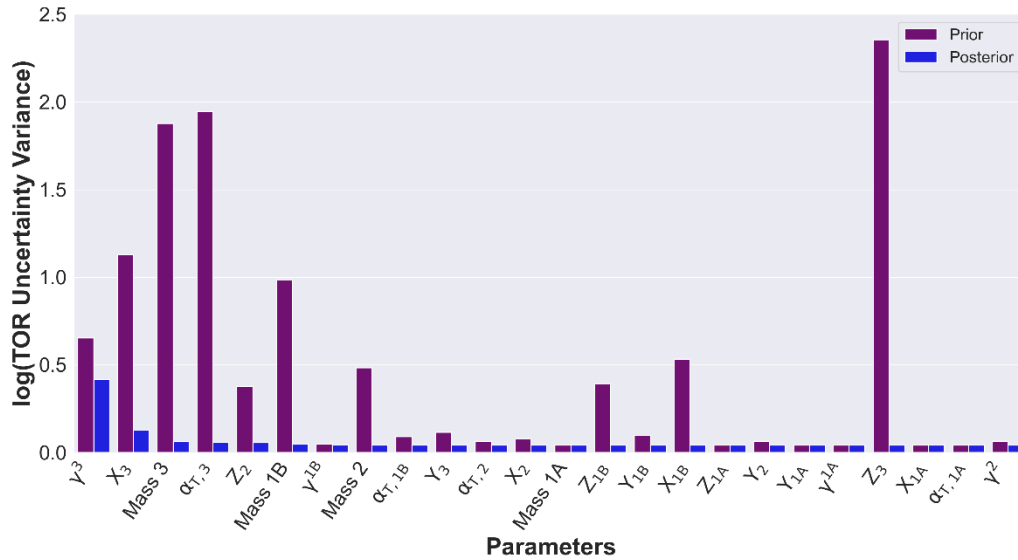
470
471
472
473
474
475
476
477
478
479
480
481
482
483
484

As indicated in Figure 8, the primary driver of posterior TOR uncertainty, γ^3 , reflected its role in regulating source discharge concentrations over several orders of magnitude. While a lack of extensive groundwater monitoring at contaminated sites could limit γ constraining via history-matching, S_a^N and flow-field heterogeneities may also pose additional uncertainties on mass transfer assumptions. In this case, TCE dissolution tailing, primarily regulated by S_3^N , was also modulated by flow channelization in the coarse sand lens (Figure 2b). Transient reductions in DNAPL interfacial areas, which limit mass transfer rates through the γ parameter, were obfuscated by a local increase in U_0 and k_r in the heterogeneous experiment (Stewart et al., 2021). Although the level of characterization detail available for the flow-cell experiment would not be available at field sites, VA modeling provides an efficient means to evaluate conceptual assumptions of system heterogeneities and quantify mass transfer uncertainties. The prior uncertainty rankings of S_{1B}^N and S_3^N parameters (Figure 8) emphasized the level of effort for DNAPL delineation required for adequate model parameterization.



485
486
487

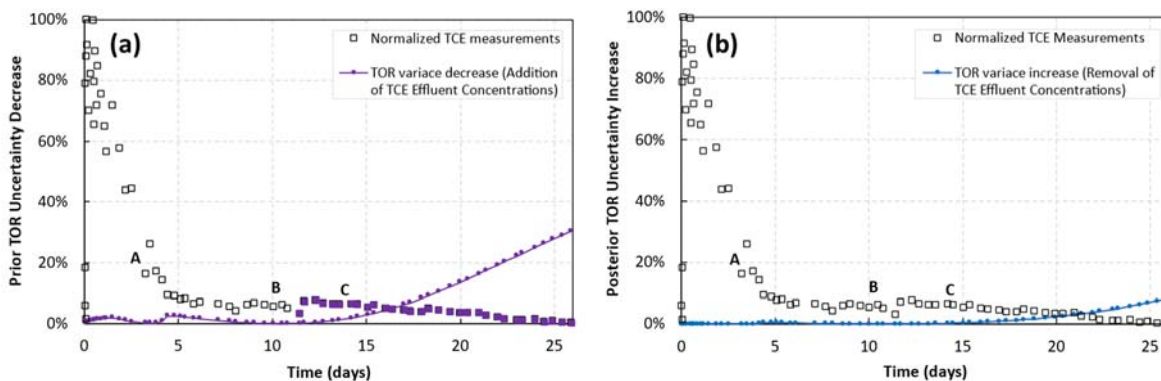
Figure 7. Prior and posterior parameter contributions to TOR uncertainty in the mixed experiment.



488 **Figure 8.** Prior and posterior parameter contributions to TOR uncertainty of heterogeneous experiment.
 489
 490

491 *4.2.3. Data-Worth Analysis*
 492

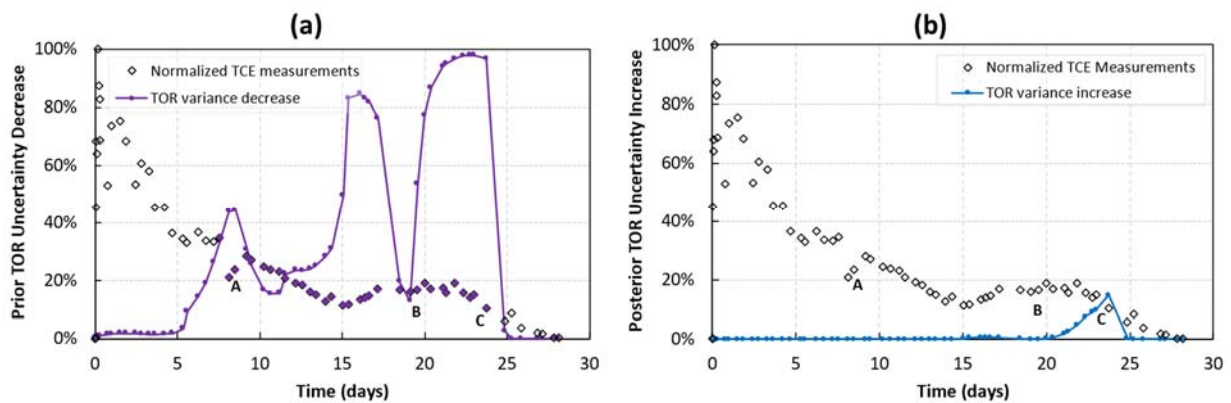
493 The worth of TCE monitoring profiles of the mixed and heterogeneous experiments is shown in
 494 Figures 9 and 10, respectively. Both figures express data worth on the Y-axis as a percent reduction
 495 and increase of σ_{TOR} and σ'_{TOR} (see Table 2), respectively, by individual monitoring
 496 measurements. Figures 9a and 10a indicate the worth of individual measurements for constraining
 497 prior TOR uncertainty (σ_{TOR}), whereas Figures 9b and 10b depict increases in posterior
 498 (constrained) TOR uncertainty (σ'_{TOR}) caused by data removal. As shown in Figure 10, a tendency
 499 of increasing data worth in the mixed experiment started at point C, when the pool mass transfer
 500 area ($A_{p,xy}$) was sufficiently reduced to onset dissolution tailing. Similar prior and posterior data-
 501 worth trends in the mixed experiment suggested that peak concentrations emanating from ganglia-
 502 dominated accumulations do not constrain TOR. In turn, the RUVR of pool mass (~70%) and $\alpha_{T,p}$
 503 (~60%) controlling TOR uncertainty was attributed to TCE monitoring after point C (Figure 9),
 504 highlighting the benefit of history-matching for characterizing sites with aged source zones and
 505 simple architectures. In these experiments, point C represents a rough mid-point for the DNAPL
 506 TOR despite an 80% reduction in the total DNAPL mass.
 507



508 **Figure 9.** Worth of monitoring data for constraining TOR uncertainty of the mixed experiment shown in Figure 2a:
 509 a) Decrease in prior uncertainty with addition of individual TCE concentrations. The filled data points highlight the
 510

511 greatest information content for reducing prior TOR uncertainty. b) Increases in posterior uncertainty with data
 512 removal. Points A, B, C show DNAPL depletion images measured by DiFilippo et al. (2010).

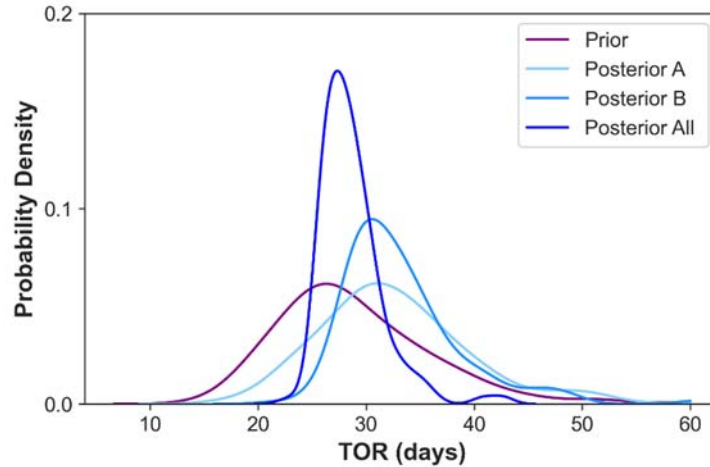
513
 514 Figure 10a shows the worth of breakthrough inflection points along the TCE monitoring curve of
 515 the heterogeneous experiment for constraining σ_{TOR} . The first peak in the σ_{TOR} decrease curve
 516 coincided with point A, indicating the onset of rapid dissolution of DNAPL mass accumulation 1b
 517 after mass 1a was completely dissolved. The second peak of σ_{TOR} reduction occurred during a
 518 slight increase in TCE concentrations, reflecting an increased k_r through mass 2 after mass 1B was
 519 dissolved. The final peaks of σ_{TOR} reduction (Figure 10a) and σ'_{TOR} increase (Figure 10b)
 520 coincided with the final stage of DNAPL dissolution associated to mass 3. These results
 521 highlighted disadvantages of predicting future system behavior from limited monitoring profiles,
 522 corresponding to situations where remaining source architectures and heterogeneities have not yet
 523 been reflected in historical dissolution trends.
 524



525
 526 **Figure 10.** Worth of TCE dissolution measurements for reducing TOR uncertainty of the heterogeneous experiment
 527 shown in Figure 2b: a) Decrease in prior uncertainty with addition of individual history-matching constraints. The
 528 filled data points highlight the greatest information content for reducing prior TOR uncertainty. b) Increases in
 529 posterior uncertainty with data loss. Points A, B, C show the DNAPL depletion measured by DiFilippo et al. (2010).
 530

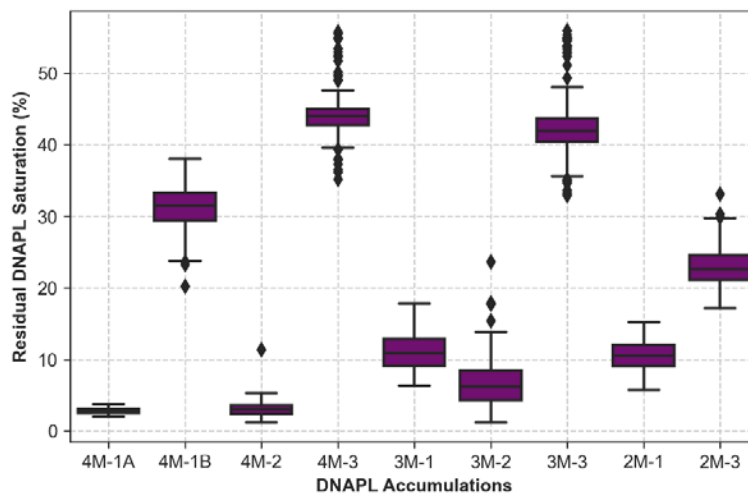
531 **4.3. Nonlinear Uncertainty Analysis**

532
 533 Figure 11 indicates that all prior and posterior source dissipation timeframes of the mixed
 534 experiment included the “true TOR” ($\mu_{TOR} = 27.9$ days). All posterior analyses underestimated the
 535 initial DNAPL mass in the mixed experiment by $\sim 11\%$, yet the known value of 17.2 g was included
 536 within 95% confidence limits (results not shown). The average estimated S_g^N and S_p^N values were
 537 4% and 40%, respectively, consistent with initial experimental conditions (Figure 2a). Prior and
 538 posterior TOR uncertainties in Figure 11 demonstrated the utility of VA modeling for estimating
 539 unbiased depletion timeframes a priori, by leveraging DNAPL-delineation or limited monitoring
 540 data pertaining to source zones with relatively simple architectures and flow conditions.
 541

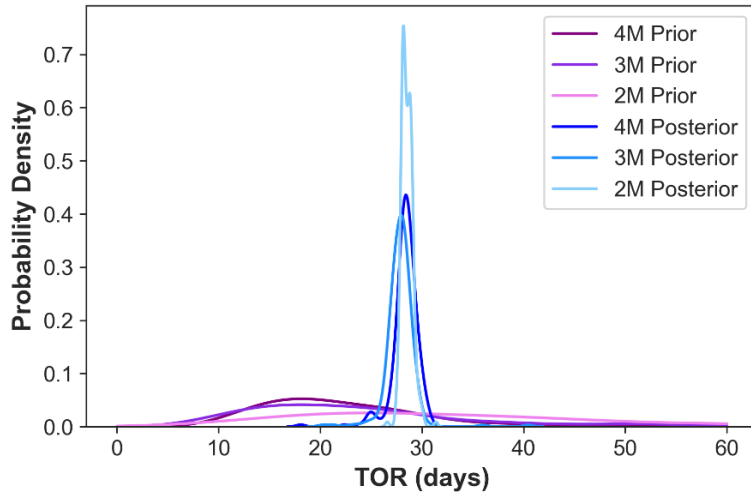


542 **Figure 11.** Prior and posterior TOR PDFs of mixed experiment. Posterior A and B were estimated by history-
 543 matching TCE concentrations through day 11.7 and 20 (Figure 10), respectively.
 544

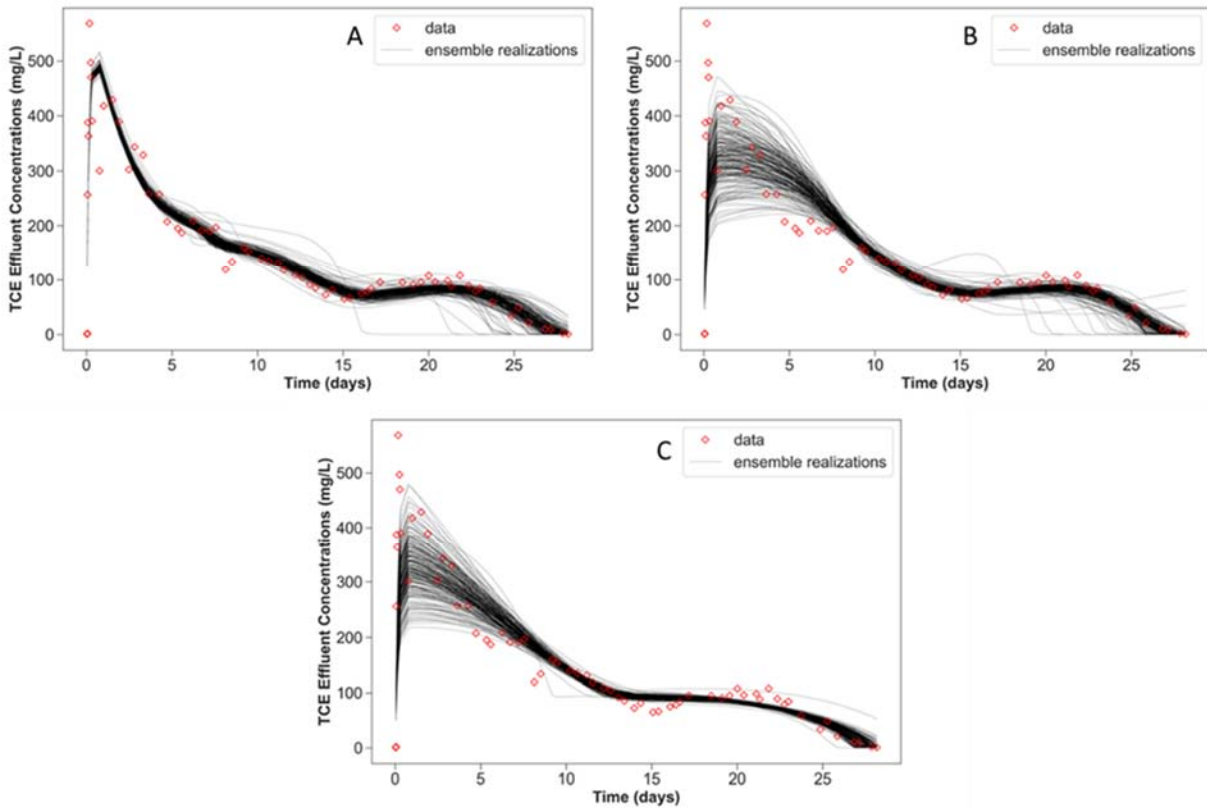
545
 546 The stochastic optimization of the heterogeneous experiment models underestimated initial
 547 DNAPL mass by $\sim 7\%$, with 95% confidence limits encompassing the injected amount of 20.4 g
 548 (results not shown). As illustrated in Figure 12, posterior S_a^N uncertainties reflected the averaging
 549 by model resolutions required to history-match the complete TCE dissolution profile and quantify
 550 TOR uncertainty (Figure 13). Figure 13 shows all posterior TOR PDFs encompassing the “true”
 551 TOR of 28.6 days, emphasizing the worth of final DNAPL dissolution stages for constraining TOR
 552 with various model resolutions. However, the 2M and 3M models required removing peak TCE
 553 concentrations from day 0 through day 9 (Figure 14). Not doing so did not impact the accuracy of
 554 estimated DNAPL mass, but resulted in an artificially low initial S_l^N of lumped mass 1 from
 555 inadequate parameterization complexity (results not shown). Sufficient source architecture
 556 parameters are thereby necessary to assimilate complex dissolution profiles to avoid misleading
 557 injection-based remedial designs.
 558



559 **Figure 12.** Posterior DNAPL saturation distributions of each DNAPL accumulation in the 4M, 3M, and 2M VA
 560 models of the heterogeneous experiment.
 561
 562



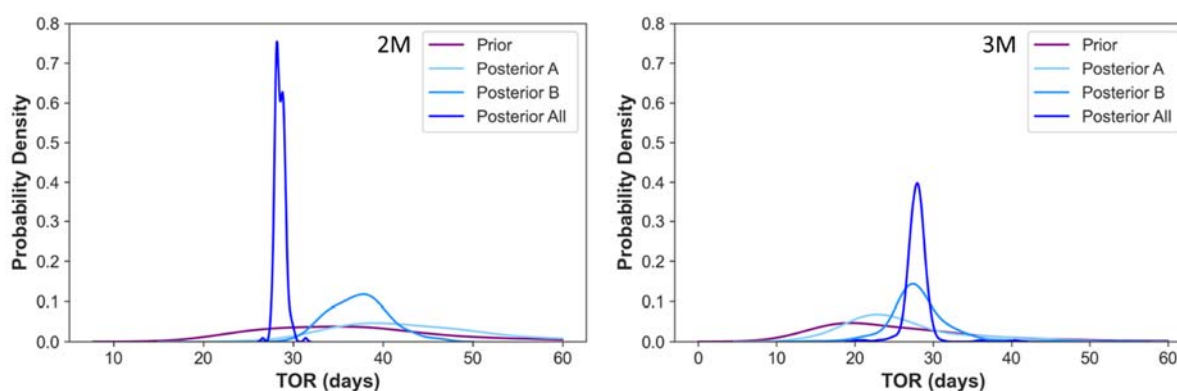
563 **Figure 13.** Prior and posterior TOR PDFs of the heterogeneous experiment conceptualized by 2, 3, and 4 DNAPL
 564 accumulations.
 565
 566
 567



568 **Figure 14.** Posterior model ensembles of the heterogeneous experiment corresponding to (A) 4, (B) 3, and (C) 2
 569 DNAPL accumulations.
 570
 571

572 Figure 15 shows prior predictive PDFs approximated with S_a^N constraints assuming availability of
 573 HRSC data to inform model parameters. The prior S_a^N constraints for this analysis correspond
 574 Figure 12. Despite low probability densities, all prior PDFs encompassed the $\mu_{TOR} = 28.6$ days,
 575 suggesting that even a low-resolution model (2M) accounting for S_a^N distributions along the flow

576 path can predict unbiased source dissipation timeframes. However, Figure 15 depicts biased
 577 posterior 2M PDFs tending to exclude μ_{TOR} resulting from monitoring data assimilation with
 578 inadequate parameterization complexity. Unlike 2M, 3M included an adjustable “dissolution
 579 enhancement factor” representing increased velocity through the coarse lens. Omitting that
 580 parameter from the 3M model (fixing it at a value of 1) did not impact σ'_{TOR} estimated from the
 581 entire TCE profile (Figures 14 and 15). However, σ_{TOR} and σ'_{TOR} estimated from partial TCE
 582 profiles were also overestimated (excluding μ_{TOR}) and the nonmonotonic increase in TCE
 583 concentrations from day 15 through day 20 could not be reproduced (results not shown). Hence,
 584 the unbiased Posterior A and B results of the 3M model, shown in Figure 15, suggested that in
 585 addition to adequate representation of DNAPL distribution along the local flow path,
 586 parameterization of flow field heterogeneity is also necessary to avoid biasing model estimates
 587 through history-matching of multistage and nonmonotonic dissolution profiles.
 588



589
 590 **Figure 15.** Probability density functions of TOR approximated with 2M and 3M models of heterogeneous experiment.
 591 Posterior A and B PDFs were estimated from partial TCE monitoring profiles through day 14 and 20, respectively.
 592

593 5. Conclusions

594
 595 This work demonstrated a practical approach for estimating DNAPL dissolution timeframes
 596 coupling upscaled modeling with uncertainty analysis methods. Assimilation of monitoring data
 597 may induce model predictive bias without sufficient parameterization complexity representing the
 598 DNAPL source, including sequential dissolution of DNAPL accumulations distributed along the
 599 flow path. In both experiments, saturation parameters and transverse dispersion of pool-dominated
 600 DNAPL accumulations controlled the source zone longevity, and were constrained by tailing of
 601 final dissolution stages despite their negligible sensitivity with respect to measured effluent
 602 concentrations. Because the VA model provides TOR as a direct output, FOSM analyses can be
 603 used to guide site characterization efforts to constrain prior, or remaining posterior parameter
 604 uncertainties responsible for predictive TOR and mass discharge/flux uncertainties. As
 605 demonstrated with the heterogeneous source zone experiment, field mapping of aquifer hydraulics,
 606 and/or estimation of source zone architecture using physically-based inversion methods can be
 607 leveraged to refine site conceptual assumptions encapsulated in VA model parameters. This
 608 includes direct constraining of transverse vertical dispersivity at the source zone scale, regardless
 609 of DNAPL saturation, differentiating its contribution to DNAPL dissolution from macrodispersion
 610 at the contaminant plume scale.
 611

612 Local groundwater velocity and source zone dimensions had a prominent impact on mass
613 discharge and DNAPL persistence because of their scaling role on mass transfer processes. Hence,
614 these parameters require constraining by monitoring and site characterization scales, promoting
615 adequate dilution and flow bypassing effects on DNAPL dissolution. Conversely, saturation
616 parameters of ganglia-dominated DNAPL accumulations, which may not be directly measured at
617 field sites, did not impact source longevity timeframes when pools were present. Yet their
618 influence on peak discharge concentrations justifies their parameterization to avoid erroneous
619 estimates of DNAPL saturation distributions and mass discharge rates. Although accurately
620 simulating mass discharge was possible with increased resolution of source zone architecture,
621 exclusive designations of ganglia and pool fractions of DNAPL may be inadequate for mass
622 transfer modeling. The high-saturation DNAPL accumulation embedded in the coarse sand lens of
623 the heterogeneous experiment, controlled the source zone longevity without dispersive mass
624 transfer. Moreover, lumping the downgradient saturations and ignoring flow field heterogeneity,
625 biased lifespan estimates of the heterogenous source zone and degraded the replication of
626 nonmonotonic DNAPL dissolution tailing. While this level of characterization detail may not be
627 available for contaminated sites, upscaled modeling and stochastic uncertainty analyses of site
628 conceptual assumptions can support risk-based decision making through data assimilation and
629 predictive hypothesis testing with a physical mass transfer basis.

630

631 **Acknowledgements**

632

633 This study was supported by the Environmental Security Technology Certification Program
634 (ESTCP) under Project ER19-5223. The content of this manuscript has not been subject to agency
635 review and does not necessarily represent the view of the sponsoring agency.

636

637 **Data Availability Statement**

638

639 A copy of the VA model executable and input instructions can be requested from Praxis
640 Environmental Tech., Inc. at <https://www.praxis-enviro.com/contact>. The SENSAN, PWTADJ2,
641 PREDUNC, GENLINPRED, and PEST software utilities used for sensitivity and linear
642 uncertainty analyses are available at <https://pesthomepage.org/programs>. The PESTPP-iES
643 software used for ensemble-based parameter estimation and nonlinear uncertainty analyses is
644 available at [https://www.usgs.gov/software/pest-software-suite-parameter-estimation-
645 uncertainty-analysis-management-optimization-and](https://www.usgs.gov/software/pest-software-suite-parameter-estimation-uncertainty-analysis-management-optimization-and) (version 5.1.6 was used and the source code
646 is available on <https://github.com/usgs/pestpp/releases/tag/5.1.6>). Except for the data-worth results
647 figures, figures in the results and discussion section were produced with the Matplotlib
648 (<https://matplotlib.org/>) version 3.5.1 and Seaborn (<https://seaborn.pydata.org/>) version 0.11.2
649 libraries using the Python programming language. Data is supplied in an excel file for peer review
650 purposes and will be archived in an online repository maintained by Virginia Tech with a unique
651 DOI number.

652

653

654

655

656

657

658 **6. References**

659

660 Abriola, L. M. (2005). Guest Editorial: Contaminant Source Zones: Remediation or Perpetual
661 Stewardship? *Environmental Health Perspectives*, *113*(7), A438-A439.
662 <https://doi.org/10.1289/ehp.113-a438>

663 Abriola, L. M., Miller, E. L., Pennell, K. D., Ramsburg, A., & Christ, J. A. (2013). *Metric*
664 *identification and protocol development for characterizing DNAPL source zone*
665 *architecture and associated plume response*. Alexandria, VA: SERDP Project ER-1612.

666 Agaoglu, B., Coptly, N. K., Scheytt, T., & Hinkelmann, R. (2015). Interphase mass transfer
667 between fluids in subsurface formations: A review. *Advances in Water Resources*, *79*, 162-
668 194. <https://doi.org/10.1016/j.advwatres.2015.02.009>

669 Arshadi, M., De Paolis Kaluza, M. C., Miller, E. L., & Abriola, L. M. (2020). Subsurface Source
670 Zone Characterization and Uncertainty Quantification Using Discriminative Random
671 Fields. *Water Resources Research*. <https://doi.org/10.1029/2019WR026481>

672 Carey, G. R., McBean, E. A., & Feenstra, S. (2018). Estimating transverse dispersivity based on
673 hydraulic conductivity. *Environmental Technology & Innovation*, *10*, 36-45.
674 <https://doi.org/10.1016/j.eti.2018.01.008>

675 Christ, J. A., Ramsburg, A. C., Pennell, K. D., & Abriola, L. M. (2006). Estimating mass discharge
676 from dense nonaqueous phase liquid source zones using upscaled mass transfer
677 coefficients: An evaluation using multiphase numerical simulations. *Water Resources*
678 *Research*, *42*(11). <https://doi.org/10.1029/2006WR004886>

679 Christ, J. A., Ramsburg, C. A., Pennell, K. D., & Abriola, L. M. (2010). Predicting DNAPL mass
680 discharge from pool-dominated source zones. *Journal of Contaminant Hydrology*, *114*(1-
681 4), 18 - 34. <https://doi.org/10.1016/j.jconhyd.2010.02.005>

682 Dekker, T. J., & Abriola, L. M. (2000). The influence of field-scale heterogeneity on the infiltration
683 and entrapment of dense nonaqueous phase liquids in saturated formations. *Journal of*
684 *Contaminant Hydrology*, *42*(2-4), 187-218. [https://doi.org/10.1016/S0169-](https://doi.org/10.1016/S0169-7722(99)00092-3)
685 [7722\(99\)00092-3](https://doi.org/10.1016/S0169-7722(99)00092-3)

686 DiFilippo, E. L., & Brusseau, M. L. (2008). Relationship Between Mass Flux Reduction and
687 Source-Zone Mass Removal: Analysis of Field Data. *Journal of Contaminant Hydrology*,
688 *98*(1-2), 22-35. <https://doi.org/10.1016/j.jconhyd.2008.02.004>

689 DiFilippo, E. L., & Brusseau, M. L. (2011). Assessment of a Simple Function to Evaluate the
690 Relationship Between Mass Flux Reduction and Mass Removal for Organic-Liquid
691 Contaminated Source Zones. *Journal of Contaminant Hydrology*, *123*(3-4), 104-113.
692 <https://doi.org/10.1016/j.jconhyd.2010.12.011>

- 693 DiFilippo, E. L., Carroll, K. C., & Brusseau, M. (2010). Impact of organic-liquid distribution and
694 flow heterogeneity on reductions in mass flux. *Journal of Contaminant Hydrology*, 115(1-
695 4), 14-25. <https://doi.org/10.1016/j.jconhyd.2010.03.002>
- 696 Doherty, J. (2015). *Calibration and Uncertainty Analysis for Complex Environmental Models*.
697 Brisbane, Australia: Watermark Numerical Computing.
- 698 Doherty, J., & Moore, C. (2020). Decision Support Modeling: Data Assimilation, Uncertainty
699 Quantification, and Strategic Abstraction. *Groundwater*, 58(3), 327-337.
700 <https://doi.org/10.1111/gwat.12969>
- 701 Eniarson, M., Fure, A., St. Germain, R., Chapman, S., & Parker, B. (2018). DyeLIF™: A New
702 Direct-Push Laser-Induced Fluorescence Sensor System for Chlorinated Solvent DNAPL
703 and Other Non-Naturally Fluorescing NAPLs. *Groundwater Monitoring & Remediation*,
704 28-42. <https://doi.org/10.1111/gwmmr.12296>
- 705 Falta, R. (2003). Modeling sub-grid-block-scale dense nonaqueous phase liquid (DNAPL) pool
706 dissolution using a dual-domain approach. *Water Resources Research*, 39(12).
707 <https://doi.org/10.1029/2003WR002351>
- 708 Finsterle, S. (2015). Practical notes on local data-worth analysis. *Water Resources Research*.
709 <https://doi.org/10.1002/2015WR017445>
- 710 Frind, E. O., Molson, J. W., & Schirmer, M. (1999). Dissolution and mass transfer of multiple
711 organics under field conditions: The Borden emplaced source. *Water Resources Research*,
712 35(3), 683-694. <https://doi.org/10.1029/1998WR900064>
- 713 Guo, Z., Russo, A. E., DiFilippo, E. L., Zhang, Z., Zheng, C., & Brusseau, M. L. (2020).
714 Mathematical modeling of organic liquid dissolution in heterogeneous source zones.
715 *Journal of Contaminant Hydrology*, 235. <https://doi.org/10.1016/j.jconhyd.2020.103716>
- 716 Horst, J., Welty, N., Stuetzle, R., Wenzel, R., & Germain, R. (2018). Fluorescent dyes: A new
717 weapon for conquering DNAPL characterization. *Groundwater Monitoring &*
718 *Remediation*, 38(1), 19-25. <https://doi.org/10.1111/gwmmr.12261>
- 719 Huang, J., Christ, J. A., & Goltz, M. N. (2010). Analytical solutions for efficient interpretation of
720 single-well push-pull tracer tests. *Water Resources Research*.
721 <https://doi.org/10.1029/2008WR007647>
- 722 ITRC (Interstate Technology & Regulatory Council). (2010). *Use and Measurement of Mass Flux*
723 *and Mass Discharge*. Washington, D.C.: Interstate Technology & Regulatory Council,
724 Integrated DNAPL Site Strategy Team. Retrieved from www.itrcweb.org
- 725 Kang, X., Kokkinaki, A., Kitandis, P. K., Shi, X., Lee, J., Mo, S., & Wu, J. (2021a).
726 Hydrogeophysical Characterization of Nonstationary DNAPL Source Zones by Integrating
727 a Convolutional Variational Autoencoder and Ensemble Smoother. *Water Resources*
728 *Research*, 57(1). <https://doi.org/10.1029/2020WR028538>

- 729 Kang, X., Kokkinaki, A., Power, C., Kitandis, P. K., Shi, X., Duan, L., . . . Wu, J. (2021b).
730 Integrating deep learning-based data assimilation and hydrogeophysical data for improved
731 monitoring of DNAPL source zones during remediation. *Journal of Hydrology*, *601*,
732 126655. <https://doi.org/10.1016/j.jhydrol.2021.126655>
- 733 Kang, X., Kokkinaki, A., Shi, X., Yoon, H., Lee, J., Kitandis, P. K., & Wu, J. (2022). Integration
734 of Deep Learning-Based Inversion and Upscaled Mass-Transfer Model for DNAPL Mass-
735 Discharge Estimation and Uncertainty Assessment. *Water Resources Research*, *58*(10).
736 <https://doi.org/10.1029/2022WR033277>
- 737 Klenk, I. D., & Grathwohl, P. (2002). Transverse vertical dispersion in groundwater and the
738 capillary fringe. *Journal of Contaminant Hydrology*, *58*(1–2), 111-128.
739 [https://doi.org/10.1016/S0169-7722\(02\)00011-6](https://doi.org/10.1016/S0169-7722(02)00011-6)
- 740 Koch, J., & Nowak, W. (2015). Predicting DNAPL mass discharge and contaminated site
741 longevity probabilities: Conceptual model and high-resolution stochastic simulation.
742 *Water Resources Research*, 806 - 831. <https://doi.org/10.1002/2014WR015478>.
- 743 Koch, J., & Nowak, W. (2016). Identification of contaminant source architectures—A statistical
744 inversion that emulates multiphase physics in a computationally practicable manner. *Water*
745 *Resources Research*, *52*, 1009–1025. <https://doi.org/10.1002/2015WR017894>
- 746 Kokkinaki, A., O'Carroll, M., Werth, C. J., & Sleep, B. E. (2013). Coupled simulation of DNAPL
747 infiltration and dissolution in three-dimensional heterogeneous domains: Process model
748 validation. *Water Resources Research*, *49*, 7023-7036.
749 <https://doi.org/10.1002/wrcr.20503>, 2013
- 750 Kokkinaki, A., Werth, C. J., & Sleep, B. E. (2014). Comparison of upscaled models for multistage
751 mass discharge from DNAPL source zones. *Water Resources Research*, 3187 - 3205.
752 <https://doi.org/10.1002/2013WR014663>
- 753 Kueper, B. H., Stroo, H. F., Vogel, C. M., & Ward, C. H. (2014). *Chlorinated Solvent Source Zone*
754 *Remediation*. Springer New York. <https://doi.org/10.1007/978-1-4614-6922-3>
- 755 Lemke, L. D., & Abriola, L. M. (2006). Modeling dense nonaqueous phase liquid mass removal
756 in nonuniform formations: Linking source-zone architecture and system response.
757 *Geosphere*, *2*(2), 74-82. <https://doi.org/10.1130/GES00025.1>
- 758 Marble, J. C., DiFilippo, E. L., Zhang, Z., Tick, G. R., & Brusseau, M. L. (2008). Application of
759 a lumped-process mathematical model to dissolution of non-uniformly distributed
760 immiscible liquid in heterogeneous porous media. *Journal of Contaminant Hydrology*,
761 *100*, 1-10. <https://doi.org/10.1016/j.jconhyd.2008.04.003>
- 762 Miller, C. T., Christakos, G., Imhoff, P. T., McBride, J. F., & Pedit, J. A. (1998). Multiphase flow
763 and transport modeling in heterogeneous porous media: challenges and approaches.
764 *Advances in Water Resources*, *21*(2), 77-120. [https://doi.org/10.1016/S0309-](https://doi.org/10.1016/S0309-1708(96)00036-X)
765 [1708\(96\)00036-X](https://doi.org/10.1016/S0309-1708(96)00036-X)

- 766 Mobile, M. A., Widdowson, M. A., & Gallagher, D. L. (2012). Multicomponent NAPL Source
767 Dissolution: Evaluation of Mass-Transfer Coefficients. *Environmental Science &*
768 *Technology*, 46(18), 10047-10054. <https://doi.org/10.1021/es301076p>
- 769 Molz, F. (2015). Advection, Dispersion, and Confusion. *Ground Water*, 53(3), 348-353.
770 <https://doi.org/10.1111/gwat.12338>
- 771 Moore, C., & Doherty, J. (2005). Role of the calibration process in reducing model predictive
772 error. *Water Resources Research*. <https://doi.org/10.1029/2004WR003501>
- 773 Parker, J. C., & Park, E. (2004). Modeling field-scale dense nonaqueous phase liquid dissolution
774 kinetics in heterogeneous aquifers. *Water Resources Research*, 2004.
775 <https://doi.org/10.1029/2003WR002807>
- 776 Powers, S. E., Abriola, L. M., & Weber Jr, W. J. (1992). An Experimental Investigation of
777 Nonaqueous Phase Liquid Dissolution in Saturated Subsurface Systems: Steady State Mass
778 Transfer Rates. *Water Resources Research*, 28(10), 2691-2705.
779 <https://doi.org/10.1029/92WR00984>
- 780 Powers, S. E., Abriola, L. M., & Weber, W. J. (1994). An experimental investigation of
781 nonaqueous phase liquid dissolution in saturated systems: Transient mass transfer rates.
782 *Water Resources Research*, 30(2), 321-332. <https://doi.org/10.1029/93WR02923>
- 783 Rockhold, M., Zhang, Z., & Bott, Y.-J. (2016). *Scale-Dependent Solute Dispersion in Variably*
784 *Saturated Porous Media*. Richland, WA: Pacific Northwest National Laboratory.
- 785 Saenton, S., & Illangasekare, T. H. (2004). Determination of DNAPL entrapment architecture
786 using experimentally validated numerical codes and inverse modeling. *Developments in*
787 *Water Science*, 55, 767-778. [https://doi.org/10.1016/S0167-5648\(04\)80098-4](https://doi.org/10.1016/S0167-5648(04)80098-4)
- 788 Saenton, S., & Illangasekare, T. H. (2007). Upscaling of mass transfer rate coefficient for the
789 numerical simulation of dense nonaqueous phase liquid dissolution in heterogeneous
790 aquifers. *Water Resources Research*, 43(2). <https://doi.org/10.1029/2005WR004274>
- 791 Stewart, L. D., Chambon, J. C., Widdowson, M. A., & Kavanaugh, M. C. (2022). Upscaled
792 modeling of complex DNAPL dissolution. *Journal of Contaminant Hydrology*, 244.
793 <https://doi.org/10.1016/j.jconhyd.2021.103920>
- 794 Tang, T. (2019). *An Adjoint-Sensitivity-Analysis Based Mathematical Framework: DNAPL Source*
795 *Zone Characterization, Uncertainty Quantification, and Sampling Strategy Design*
796 (Doctoral dissertation). Civil and Environmental Engineering. Ann Arbor, MI: Tufts
797 University. Retrieved from ProQuest (Access provided by University Libraries through
798 Virginia Tech)
- 799 Watermark Numerical Computing. (2018). *Model-Independent Parameter Estimation. User*
800 *Manual Part II: PEST Utility Support Software*.
- 801 White, J. T. (2018). A model-independent iterative ensemble smoother for efficient history-
802 matching and uncertainty quantification in very high dimensions. *Environmental*

1 Quantifying DNAPL source zone longevity with upscaled modeling: practical 2 insights from flow-cell experiments and uncertainty analyses

3
4 Andres E. Prieto-Estrada¹, Mark A. Widdowson¹, and Lloyd D. Stewart²

5
6 ¹ The Charles E. Via, Jr. Department of Civil and Environmental Engineering, Virginia Tech,
7 Blacksburg, Virginia 24061-0105, United States

8 ² Praxis Environmental Technologies, Inc., 1440 Rollins Road, Burlingame, California 94010,
9 United States

10
11 Corresponding author, e-mail address: mwiddows@vt.edu (M.A. Widdowson)

12 13 Key Points

- 14
15 • Upscaled modeling and uncertainty analyses of flow-cell experiments elucidated upon data
16 assimilation strategies at DNAPL sites
- 17 • Parameterization of source zone heterogeneities for history-matching was necessary to
18 predict unbiased DNAPL dissolution timeframes
- 19 • Coarse DNAPL delineation sufficed to quantify unbiased uncertainty limits of source zone
20 lifespans a priori

21 Abstract

22 Estimating dissipation timeframes and contaminant mass discharge rates of dense non-aqueous
23 phase liquids (DNAPLs) source zones is of key interest for environmental-management support.
24 Upscaled mathematical modeling of DNAPL dissolution provides a practical approach for
25 assimilating site characterization and downgradient monitoring data to constrain future system
26 behavior. Yet significant uncertainties on predictions of source zone dissipation rates may arise
27 from inadequate or inaccurate conceptual assumptions in parameterization designs. These
28 implications were investigated through upscaled modeling, sensitivity, and uncertainty analyses of
29 high-resolution flow-cell experiments. Sensitivity results emphasized the role of local groundwater
30 velocity and source dimensions in mass transfer scaling by strongly influencing error with respect
31 to DNAPL persistence and dissolution rates. Linear uncertainty analyses, facilitated by PEST
32 ancillary software, demonstrated the worth of monitoring profiles for constraining DNAPL
33 saturations and dispersive mass transfer rates, responsible for source zone longevity. Nonlinear
34 analyses performed with the iterative ensemble smoother PESTPP-iES, facilitated the
35 quantification of unbiased source dissipation uncertainties from DNAPL delineation data.
36 Conversely, monitoring data assimilation without consideration of flow-field heterogeneity and
37 saturation distribution along the flow path biased model predictions. Our analyses provided
38 practical recommendations on upscaled model design to assimilate available site data and support
39 remedial-decision making.

40 41 Plain Language Summary

42 Currently, remedial-decision makers rarely benefit from physically-based modeling methods and
43 uncertainty analyses to manage sites impacted by DNAPL source zones. Difficulties in estimating

44 DNAPL dissolution rates stem from source zone heterogeneities, which are difficult to characterize
45 in detail, compounded by a lack of scalable methodologies connecting source zone characterization
46 with discharge monitoring. In addition, monitoring and site characterization efforts supporting
47 performance-based remedial objectives are typically uninformed by uncertainty evaluations
48 predicated on DNAPL mass transfer processes. To bridge that gap, we investigated the impact of
49 data-driven conceptual assumptions on predictions of source zone behavior by coupling a practical
50 DNAPL dissolution model with uncertainty quantification methods. Simulations of flow-cell
51 experiments demonstrated the worth of DNAPL delineation for constraining source zone
52 dissipation uncertainties, estimated a priori through parameterization of DNAPL distributions. In
53 turn, parameterizing system heterogeneities in greater detail was necessary to estimate unbiased
54 source zone characteristics and lifespans, derived from the assimilation of complex DNAPL
55 dissolution trends observed in monitoring profiles. Our results demonstrated how available site
56 data can be integrated into a decision-support modeling framework to inform data collection
57 strategies and remedial designs.

58

59 **Index Terms and Keywords**

60

61 Source zone persistence, source zone heterogeneity, DNAPL dissolution rates, conceptual
62 assumptions, data assimilation, model parameterization, remedial-decision making, practical
63 recommendations

64

65 **1. Introduction**

66

67 Mathematical modeling can provide valuable insights for decision support at hazardous waste sites
68 with groundwater impacted by dense non-aqueous phase liquids (DNAPLs). However, a gap
69 between simplistic analytical screening models and overly complex numerical simulators has
70 limited their applicability for estimating DNAPL longevity and dissolution rates. Researchers have
71 focused on estimating distributions of DNAPL saturation, referred to as the source zone
72 architecture, or DNAPL dissolution rates from synthetically-generated datasets using several
73 mathematical approaches to simulating mass transfer. Several studies considered either a local
74 equilibrium assumption (LEA) or Gilland-Sherwood models of interphase mass transfer (Kang et
75 al. 2021a; Powers et al., 1992, 1994; Saenton & Illangasekare, 2004).

76

77 Decision-support modeling incorporating LEA is questionable because heterogeneity of aquifer
78 hydraulic properties and source architecture can induce flow bypassing and mass transfer rate
79 limitations, resulting in nonequilibrium concentrations typically observed at field sites (Falta,
80 2003; Kokkinaki et al., 2013). Similarly, Gilland-Sherwood models rely on correlations between
81 empirical coefficients and soil particle sizes that were determined under specific bench-scale
82 conditions, which may not be applicable to field-scale problems with different hydraulic properties
83 (Powers et al., 1992; Saenton & Illangasekare, 2007). Moreover, the computational cost of pore-
84 scale numerical models incorporating LEA and Gilland-Sherwood correlations limits their
85 practicality for data assimilation and uncertainty quantification (Falta, 2003; Kokkinaki et al.,
86 2013; Powers et al., 1994). An alternative method is predicated on a lumped-process, scale-
87 dependent mass transfer coefficient estimated from monitoring data (Guo et al., 2020; Mobile et
88 al., 2012; Park & Parker, 2005). However, estimating mass transfer rates exclusively from

89 historical monitoring may bias predictions of source longevity because of architectural changes.
90 For example, early in the life cycle of a DNAPL source zone, the contributions of slowly dissolving
91 pools governing complete depletion may not be discernible in discharge data (Abriola et al., 2013).

92
93 Multistage DNAPL dissolution, typically observed at contaminated sites and in dissolution
94 experiments, arises from heterogeneity of source zone architecture (Figure 1) primarily comprised
95 by residual ganglia and high-saturation DNAPL pools (Christ et al., 2010; Dekker & Abriola,
96 2000; DiFilippo & Brusseau, 2008; Lemke & Abriola, 2006; Parker & Park, 2004). Consequently,
97 a number of high-resolution site characterization (HRSC) technologies have been developed
98 (Einarson et al., 2018; Horst et al., 2018; Kueper et al., 2014). Delineation of DNAPLs comprised
99 by chlorinated ethenes is possible with dye-enhanced laser induced fluorescence (DyeLIF) and
100 confirmatory sampling, and with indirect observation methods, such as multilevel monitoring and
101 groundwater extraction systems, passive flux meters, push-pull tracer tests, etc. (Horst et al. 2018;
102 Huang et al. 2010; ITRC, 2010; Kueper et al., 2014). Although HRSC may help constrain DNAPL
103 distribution, quantifying residual mass and saturation directly is not possible (Einarson et al.,
104 2018). Thus, inverse modeling techniques have been applied to quantify lumped-process mass
105 transfer coefficients from monitoring data Marble et al., 2008; Mobile et al., 2012; Saenton &
106 Illangasekare, 2004), or to estimate source zone architectures from borehole and geophysical
107 measurements using physically-based parameterization mechanisms (Kang et al. 2021a, 2021b).
108 Kang et al. (2022) demonstrated a novel Bayesian inversion framework to reconstruct complex
109 permeability and DNAPL saturation fields, subsequently parameterizing an upscaled model of
110 DNAPL dissolution to reproduce experimental source depletion trends.

111
112 Upscaled (domain-averaged) models lacking a physical mass transfer basis cannot assimilate
113 HRSC data and have proved ineffective at explaining and predicting DNAPL dissolution behavior
114 (Christ et al., 2006; Kokkinaki et al., 2014; Marble et al., 2008). However, upscaled models
115 incorporating metrics describing the source zone architecture, such as the ganglia-to-pool (GTP)
116 mass ratio, have shown improved success (Abriola et al. 2013; Christ et al., 2010; DiFilippo &
117 Brusseau, 2011). Stewart et al. (2021) developed a volume-averaged (VA) model of DNAPL
118 dissolution predicated on characteristic length scales of DNAPL accumulations and their relative
119 location along groundwater flow paths, explicitly accounting for mass transfer processes at the
120 source zone scale (Figure 1). The model accurately reproduced complex DNAPL dissolution
121 observed in laboratory, numerical, and field experiments by parameterizing initial, and estimable
122 system characteristics without undertaking history-matching. The VA model is therefore able to
123 assimilate HRSC and/or monitoring data to estimate source dissipation timeframes with
124 computational efficiency in a scalable and physically-based manner. Such capabilities make the
125 VA model suitable for evaluating site conceptual assumptions and quantifying uncertainties, which
126 is necessary for effective remedial-decision support (Abriola, 2005).

127
128 The primary objectives in this work were to (i) identify the relative contribution of VA mass
129 transfer parameters to source zone dissipation uncertainties, and (ii) investigate how model
130 parameterization influences predictive bias through monitoring data assimilation. The VA DNAPL
131 dissolution model developed by Stewart et al. (2021) was coupled with sensitivity and uncertainty
132 analysis methods to evaluate the worth of direct and indirect source zone measurements for
133 constraining system parameters and model uncertainty. High-resolution datasets of two DNAPL
134 dissolution experiments were leveraged to evaluate data-driven conceptual assumptions on

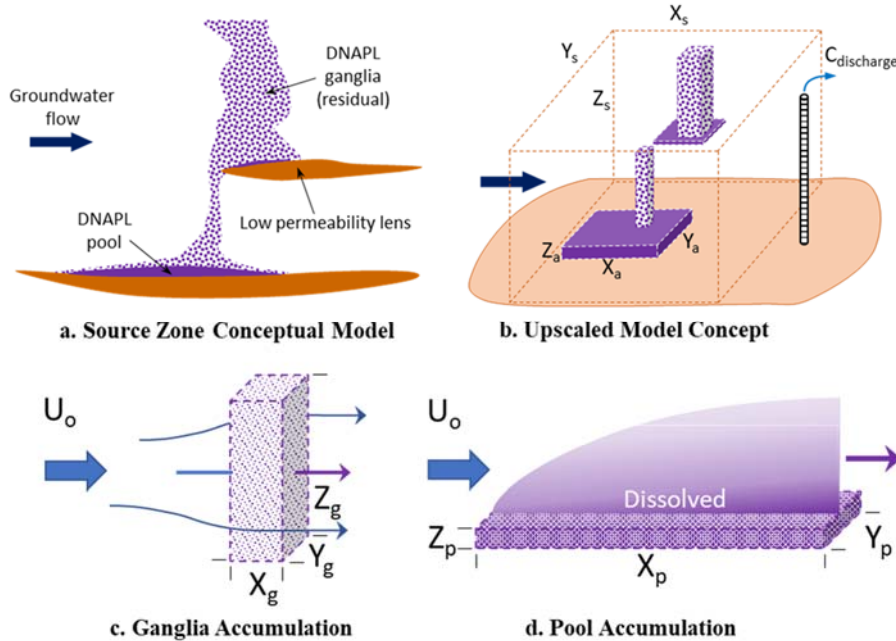
135 modeling outcomes. Our findings elucidate on model design to quantify unbiased DNAPL
 136 persistence uncertainties, yielding recommendations on HRSC and monitoring data assimilation
 137 for constraining future source zone behavior.

138 2. Upscaled and Volume-Averaged Model of DNAPL Dissolution

139
 140 Volume-averaging relaxes the need to specify precise locations of DNAPL accumulations within
 141 a finely discretized domain. The approach facilitates the incorporation of physically-based mass
 142 transfer relationships for complex field-scale dissolution behavior with computational efficiency.
 143 As presented by Stewart et al. (2021), dissolution of a single DNAPL accumulation, defined as a
 144 volume of relative uniformity in saturation, can be simulated by a generalized upscaled mass
 145 transfer function:

$$k_a = \frac{U_0}{V_s} \left[A_{a,yz} k_r(m_a) + A_{a,xy} \sqrt{\frac{4\alpha_T}{\pi X_a}} \left(\frac{m_a}{m_{a,0}} \right)^\gamma \right] \quad (1)$$

147



148
 149 **Figure 1.** Conceptual and volume-averaged model representations (a and b, respectively) of a DNAPL source zone
 150 comprised by characteristic accumulations of (c) residual ganglia and (d) pools. Adapted from Stewart et al. (2021).
 151

152 Where interphase mass transfer (k_a^N) from an individual DNAPL accumulation “a” is driven by
 153 the local Darcy groundwater velocity (U_0) upscaled by a source zone reference volume (V_s)
 154 encompassing the DNAPL masses. The term on the left inside the brackets represents dissolution
 155 attributable to through flow (Figure 1c), which is proportional to the projected area facing flow
 156 ($A_{a,yz} = Y_a Z_a$) of “a”. Flow through “a” is regulated by the soil relative permeability (k_r) which
 157 gradually increases the DNAPL dissolution rate as the DNAPL volume is reduced. The term on
 158 the right represents dissolution attributable to dispersion into bypassing flow (Figure 1d), which is
 159 proportional to the hydrodynamic transverse dispersivity (α_T) around “a” and the horizontal area
 160 of the accumulation ($A_{a,xy} = X_a Y_a$). Mass dissolution from low DNAPL saturations, i.e., ganglia,

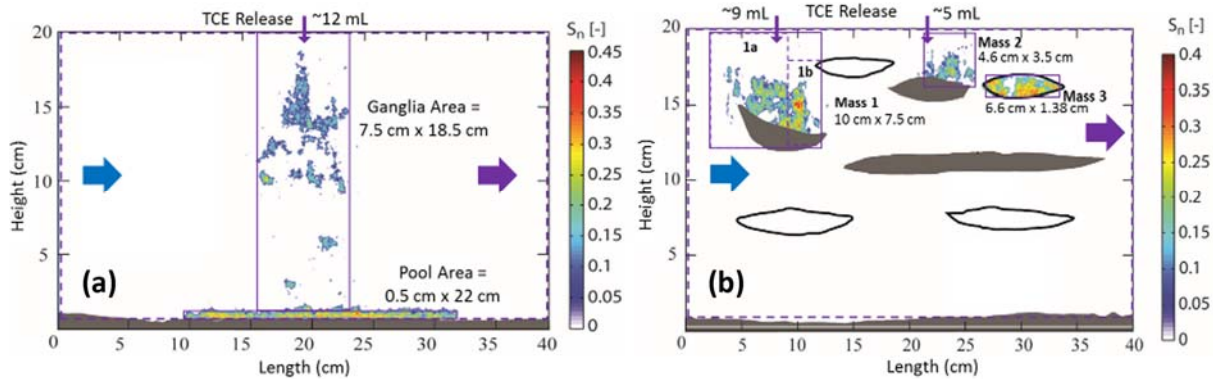
161 are dominated by flow through, while high saturation zones, i.e., pools, can be dominated by
 162 dispersion. The normalized mass (m/m_0) term reflects a transient reduction of DNAPL interfacial
 163 area. Theoretically, the dimensionless exponent $\gamma = 2/3$ for ganglia-dominated accumulations, and
 164 $\gamma = 1/2$ for pool-dominated accumulations. The γ exponent may be adjusted during model history-
 165 matching to allow for deviations from conceptual mass transfer assumptions but is expected to fall
 166 within this relatively narrow range (Stewart et al., 2021).

168 **2.1. Simulation of DNAPL Dissolution Experiments**

169
 170 Flow-cell experiments presented by DiFilippo et al. (2010) and analyzed by Guo et al. (2020) with
 171 a simplified inverse modeling method were utilized in this study. Stewart et al. (2021) simulated
 172 these experiments with the VA approach by explicitly accounting for DNAPL saturation
 173 distributions, flow field characteristics, and soil properties. The dissolution experiments consisted
 174 of two source zone scenarios: a “mixed” DNAPL architecture comprised by a ganglia-dominated
 175 accumulation and a pool-dominated accumulation in homogeneous sand, and multiple DNAPL
 176 accumulations in a “heterogeneous” soil. Details of model conceptualization and simulation results
 177 were presented in Stewart et al. (2021).

179 *2.1.1. Mixed DNAPL Architecture*

180
 181 The “mixed” source zone experiment conducted by DiFilippo et al. (2010) consisted of a uniform
 182 pack of sand (40/50 mesh) with a 2-cm thick capillary barrier located along the bottom of the test
 183 cell (Figure 2a). An injection of ~12 milliliters of trichloroethene (TCE) at the top of the test cell
 184 followed by 48-hour period prior to flow initiation generated a stable source zone architecture
 185 consisting of a vertical ganglia zone underlain by a pool. The DNAPL saturation distribution was
 186 characterized using a light reflection visualization (LRV) method and TCE effluent concentrations
 187 were monitored until source zone depletion.



189
 190 **Figure 2.** Model conceptualizations of the flow-cell experiments: (a) mixed source zone architecture and (b)
 191 heterogeneous source zone. Sub-volumes (purple rectangles) correspond to DNAPL accumulations with distinct
 192 saturations encompassed by the source volume (purple dashed line). Adapted from Stewart et al. (2021).

194 *2.1.2. Multiple DNAPL accumulations in Heterogeneous Soil*

195
 196 The test cell of the heterogeneous source experiment (Figure 2b) consisted of a matrix of
 197 homogeneous sand (40/50 mesh) with coarser (20/30 mesh) and finer (70/100 mesh) lenticular

198 zones (DeFilippo et al., 2010; Guo et al., 2020). An injection of ~15 milliliters of TCE at the top
 199 of the cell was distributed between two ports with 66% in the far left (upgradient) port and 33% in
 200 the center (downgradient) port (DeFilippo et al. 2010). The central release generated two distinct
 201 accumulations: one above a fine-grained lens and one within a coarse-grained lens. The coarse
 202 lens had an intrinsic permeability approximately 3.5 times higher than the surrounding bulk sands
 203 (DeFilippo et al., 2010), resulting in a higher velocity through this material than in the surrounding
 204 matrix. As shown in Figure 2b, Stewart et al. (2021) subdivided the upgradient accumulation into
 205 two accumulations on the basis of characteristic saturations to accurately capture the measured
 206 TCE effluent breakthrough. Sequential dissolution inhibition was also implemented by Stewart et
 207 al. (2021) for the two downgradient accumulations on the basis of their relative locations along the
 208 flow path. Nomenclature for variables in the model are presented in Table 1.

209
210 **Table 1.** Nomenclature of input parameters used in the VA model of the flow-cell experiments.

Parameter	Mixed Source		Heterogeneous Source				Unit
Mass	<i>Mass G.</i>	<i>Mass P.</i>	<i>Mass 1A</i>	<i>Mass 1B</i>	<i>Mass 2</i>	<i>Mass 3</i>	g
Length	X_g	X_p	X_{1A}	X_{1B}	X_2	X_3	m
Width	Y_g	Y_p	Y_{1A}	Y_{1B}	Y_2	Y_3	m
Height	Z_g	Z_p	Z_{1A}	Z_{1B}	Z_2	Z_3	m
NAPL Saturation	S_g^N	S_p^N	S_{1A}^N	S_{1B}^N	S_2^N	S_3^N	%
Area Facing Flow	YZ_g	YZ_p	YZ_{1A}	YZ_{1B}	YZ_2	YZ_3	m ²
Dispersive Area	XY_g	XY_p	XY_{1A}	XY_{1B}	XY_2	XY_3	m ²
Dispersivity	$\alpha_{T,g}$	$\alpha_{T,p}$	$\alpha_{T,1A}$	$\alpha_{T,1B}$	$\alpha_{T,2}$	$\alpha_{T,3}$	m
γ	γ^g	γ^p	γ^{1A}	γ^{1B}	γ^2	γ^3	-

211
212 **2.2. Sensitivity Analysis**
213
214 Model output variability was evaluated with local sensitivity analysis by systematically perturbing
215 input parameters around reference values conceptualized in Stewart et al. (2021). The goal was to
216 compare relative sensitivities with respect to measured discharge concentrations and with respect
217 to the time required to reach cleanup concentrations, defined here as time of remediation (TOR).
218 Both metrics were evaluated using the same model input variability around base parameter sets.
219 Because the plausible variability range of some parameters and their corresponding outputs differs
220 by orders of magnitude compared to those of other parameters, sensitivity coefficients were scaled
221 by maximum values to provide a relative comparison metric of simulation error. All sensitivity
222 analyses were automated coupling SENSAN and PEST software (Watermark Numerical
223 Computing, 2018) for calculation fidelity.

224
225 *2.2.1. Sensitivities with respect to TCE discharge concentrations*
226

227 Normalized sensitivity coefficients (X_{TCE}) were calculated on the basis of root mean squared errors
228 (RMSE) between simulated (sim_i) and measured (obs_i) discharge concentrations as:

$$X_{TCE} = \left(\frac{|\partial RMSE| / RMSE(a)}{|\Delta a / a|} \right) / X_{TCE}^{max} \quad (2)$$

230
231 where:

232

$$RMSE = \left[\frac{1}{N} \sum_{i=1}^N (sim_i - obs_i)^2 \right]^{1/2} \quad (3)$$

233

$$\partial RMSE = RMSE(\Delta a) - RMSE(a) \quad (4)$$

234

235 a = base parameter; Δa = perturbed parameter – a ; N = number of TCE effluent measurements. All
 236 sensitivity coefficients were normalized by maximum values (X_{TCE}^{max}) to provide a relative
 237 comparison metric of model sensitivities.

238

239 2.2.2. Sensitivities with respect to TOR

240

241 Provided with a cleanup concentration input, the VA model calculates the time required to reach
 242 the target value (e.g., contaminant MCL). Using the base parameter sets, which reflect detailed
 243 experimental conditions and initial source zone properties, TOR was calculated for both
 244 experiments setting target concentrations at $C = 0.005$ mg/L. Sensitivity coefficients normalized
 245 by maximum values (X_{TOR}^{max}) were calculated as:

246

$$X_{TOR} = \left(\frac{RMSE(\Delta a)}{|\Delta a / a|} \right) / X_{TOR}^{max} \quad (5)$$

247 3. Uncertainty Analysis

248

249 Source zone metrics controlling field-scale dissolution include DNAPL mass and distribution
 250 (Abriola et al., 2013). Uncertainties associated to both metrics can therefore propagate to model
 251 predictive uncertainties (Abriola, 2005; Tang, 2019). Prior (pre-history matching) parameter and
 252 predictive uncertainties can be informed by expert knowledge and/or by site characterization (e.g.,
 253 DNAPL delineation, projected flow through area), whereas posterior (post-history matching)
 254 uncertainties may be reduced and quantified through history-matching of monitoring data.
 255 Because volume-averaging eliminates spatial parameter correlations, the prior uncertainty of mass
 256 transfer parameters was expressed through statistically uncorrelated uncertainty bounds (archived
 257 data file). All initial (mean) parameter values were inherited from Stewart et al. (2021).

258

259 Uncertainty bounds of characteristic dimensions (V_a) and mass (m_a) of DNAPL accumulations
 260 were designed so that $1\% < S_a^N < 60\%$ and $\sum V_a < V_S$ in both experiments; where DNAPL saturation
 261 (S_a^N) of the pore space (ϕ) is also a function of DNAPL density (ρ_n) as indicated by Equation 6.
 262 Per sensitivity results, upscaling parameters (V_S , U_0 , and ϕ) were assumed well constrained by the
 263 monitoring scale and removed from predictive uncertainty evaluations. Uncertainty analyses were
 264 focused on m_a , V_a , α_T , and γ pertaining to each DNAPL accumulation. Linear and nonlinear
 265 uncertainty quantification methods were implemented to understand drivers of model uncertainties
 266 and bias emerging from data-driven conceptual assumptions.

267

$$S_a^N = \frac{m_a}{V_a \phi \rho_n} \quad (6)$$

268

269 **3.1. Linear Analysis Methods**

270

271 Model linearization expressed in Equation 7 is the primary assumption in first-order second-
 272 moment (FOSM) analysis (Doherty, 2015). Equation 7 indicates that a vector of measurements of
 273 system state \mathbf{h} equals the action of the model \mathbf{Z} on a vector of parameters \mathbf{k} plus a vector of
 274 measurement noise $\boldsymbol{\varepsilon}$. Prior model uncertainty was expressed by Equation 8 assuming a multi-
 275 gaussian probability density function (PDF), defined by mean parameter values $\underline{\mathbf{k}}$ and a diagonal
 276 covariance matrix $\mathbf{C}(\mathbf{k})$. Likewise, FOSM analysis assumes a multi-gaussian PDF of $\boldsymbol{\varepsilon}$ (Equation
 277 9), defined by mean values of zero and a diagonal covariance matrix $\mathbf{C}(\boldsymbol{\varepsilon})$. Jacobian matrices \mathbf{Z}
 278 were weighted by the inverse of the standard deviation (σ) of $\boldsymbol{\varepsilon}$. The misfit between simulated
 279 (Stewart et al., 2021) and measured TCE concentrations was used to define $\boldsymbol{\varepsilon}$, where $\sigma_{\boldsymbol{\varepsilon}}^{-1}$ values
 280 were calculated with the PEST-based utility PWTADJ2 (Watermark Numerical Computing, 2018)
 281 as observations weights for FOSM analyses.

282

$$\mathbf{h} = \mathbf{Z}\mathbf{k} + \boldsymbol{\varepsilon} \quad (7)$$

283

$$\mathbf{k} \sim \mathbf{N}[\underline{\mathbf{k}}, \mathbf{C}(\mathbf{k})] \quad (8)$$

284

$$\boldsymbol{\varepsilon} \sim \mathbf{N}[\mathbf{0}, \mathbf{C}(\boldsymbol{\varepsilon})] \quad (9)$$

285

$$s = \mathbf{y}^t\mathbf{k} \quad (10)$$

286

$$\sigma_s^2 = \mathbf{y}^t\mathbf{C}(\mathbf{k})\mathbf{y} \quad (11)$$

287

$$\mathbf{C}'(\mathbf{k}) = \mathbf{C}(\mathbf{k}) - \mathbf{C}(\mathbf{k})\mathbf{Z}^t[\mathbf{Z}\mathbf{C}(\mathbf{k})\mathbf{Z}^t + \mathbf{C}(\boldsymbol{\varepsilon})]^{-1}\mathbf{Z}\mathbf{C}(\mathbf{k}) \quad (12)$$

288

$$\sigma'_s{}^2 = \mathbf{y}^t\mathbf{C}'(\mathbf{k})\mathbf{y} \quad (13)$$

289

290 Linearization of a model prediction s (Equation 10) depends on a vector of sensitivities of s (TOR)
 291 with respect to \mathbf{k} , where the prior variance of s (Equation 11) is obtained through covariance
 292 propagation (Doherty, 2015). The posterior parameter covariance matrix (Equation 12), obtained
 293 by history-matching conditioning, was used to estimate posterior TOR uncertainty variance
 294 (Equation 13). All parameters were log-transformed to reduce their nonlinearity with respect to
 295 model outputs. Linear analyses were performed with the utility programs GENLINPRED and
 296 PREDUNC (Watermark Numerical Computing, 2018) to understand how TCE monitoring profiles
 297 constrain source zone properties, and thereby, TOR uncertainties.

298

299 *3.1.1. Relative parameter uncertainty variance (RUVR) reduction*

300

301 This statistical metric was used to evaluate the ability of dissolved TCE concentrations to reduce
 302 the prior uncertainty variance (σ_i^2) of each parameter (i) encapsulated in $\mathbf{C}(\mathbf{k})$. Equation 14 defines
 303 this metric upon extracting posterior parameter uncertainty variances ($\sigma'_i{}^2$) from $\mathbf{C}'(\mathbf{k})$ as:

304

$$RUVR_i = 1 - \frac{\sigma'_i{}^2}{\sigma_i^2} \quad (14)$$

305

306 3.1.2. Prior and posterior parameter contributions to predictive uncertainty

307
308 The contribution of an individual parameter to the uncertainty of a prediction is defined as the fall
309 of predictive uncertainty resulting from acquiring perfect knowledge of the parameter (Doherty,
310 2015). Hence, individual parameters were systematically removed from FOSM calculations to
311 investigate their relative contributions to TOR uncertainty. Because history-matching information
312 may be shared between several model parameters, the posterior contribution of a parameter could
313 increase in relation to its prior contribution, indicating a correlation with another parameter
314 (Doherty, 2015). While sensitivity analyses were useful to examine relative model error incurred
315 by perturbing individual parameters, considering parameter correlations for TOR uncertainty
316 estimation allowed assessing the worth of HRSC over history-matching for constraining the
317 models.

318 319 3.1.3. Data-Worth Analysis

320
321 The ability of spatial or temporal data to reduce the uncertainty of model predictions defines its
322 worth (Doherty & Moore, 2020; Finsterle, 2005). The worth of individual measurements of TCE
323 concentrations was quantified to understand how monitoring profiles reduce TOR uncertainty.
324 Data-worth analyses were also tied to parameter RUVR, further elucidating upon the additional
325 benefit of HRSC for constraining remaining model uncertainties.

326 327 3.2. Nonlinear Analysis Methods

328
329 Posterior TOR uncertainties were quantified using the iterative ensemble smoother PESTPP-iES
330 (White et al., 2020). Multi-gaussian prior parameter PDFs were defined by uncertainty bounds
331 spanning $\pm 2\sigma$ from initial (mean = μ) values, representing 95% confidence intervals. PESTPP-
332 iES undertakes Monte-Carlo sampling of parameter uncertainty bounds generating model
333 realizations (ensembles) which are upgraded with the Gauss-Levenberg-Marquardt (GLM)
334 optimization algorithm. Rather than simply fitting simulation results to data, PESTPP-iES can
335 generate observation ensembles considering multi-gaussian PDFs of ε (White, 2018). Here, all
336 experimental TCE concentrations were assigned an observation weight value of 1 with $\sigma_\varepsilon = 10$
337 mg/L, to simultaneously estimate model parameters and quantify the nonlinear uncertainty of TOR
338 in a stochastic manner. This approach was implemented to evaluate TOR uncertainties and bias
339 arising from source zone conceptual assumptions driven by data availability.

340
341 In practice, HRSC data may help constrain source zone architecture, and thereby model
342 conceptualizations. However, high predictive uncertainties may remain because of the inability to
343 directly measure DNAPL mass and S_a^N . The benefit of data assimilation for constraining model
344 uncertainties was investigated by estimating m_a , V_a , $\alpha_{T,a}$, and γ^a parameters in both experiments
345 from partial and complete monitoring profiles. The resulting source dissipation timeframes were
346 referred to as Posterior A (~13 days of monitoring), Posterior B (20 days) and Posterior All (26
347 days). Additionally, the heterogeneous experiment was conceptualized with 2 (2M), 3 (3M) and 4
348 (4M) DNAPL accumulations to examine TOR uncertainty and bias induced by history-matching
349 of the entire TCE monitoring profile. The 2M model included “mass 1” and lumped “mass 2” and
350 “mass 3” into a single accumulation (2M-3) based on the two release points, while the 3M model
351 included those 3 distinct DNAPL accumulations. The 4M model subdivided “mass 1” into 1A and

352 1B (Figure 2b). Except for the 2M Model, the 3M and 4M models included an enhanced dissolution
353 parameter to represent flow channelization through the coarse lens in which “mass 3” was
354 embedded. Following a variability range reported in the literature (Klenk & Grathwohl, 2002), the
355 prior uncertainty bounds of α_T parameters were defined as $5e^{-4} < \alpha_T \text{ (m)} < 2e^{-3}$ in both experiments,
356 except for $0 (1e^{-15}) < \alpha_{T,3} \text{ (m)} < 0.002$ in the coarse sand lens of the heterogeneous experiment,
357 where $\alpha_{T,3} = 0$ m provided the best match to measured TCE concentrations (Stewart et al., 2021).

358 4. Results and Discussion

359

360 4.1. Sensitivity Analysis

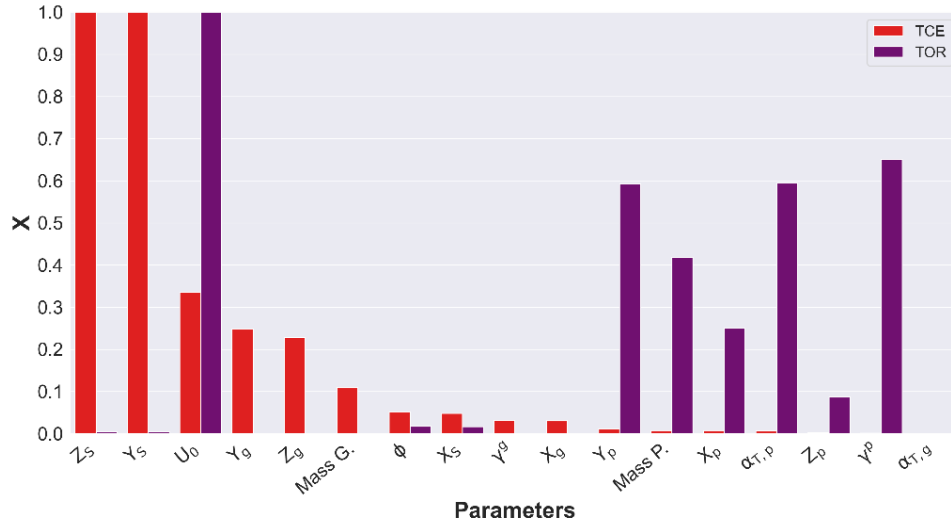
361

362 As shown in Figures 3 and 4, the greatest model sensitivities with respect to matching TCE
363 concentrations (X_{TCE}) corresponded to the source zone area (Z_S and Y_S) orthogonal to the flow
364 direction and groundwater velocity (U_θ). The former accounts for any dilution in the monitoring
365 scale, while the latter had a prominent impact on TOR in both experiments. The role of V_S and U_θ
366 on scaling mass transfer processes emphasized the need to constrain them by the monitoring scale
367 to avoid model errors induced by data assimilation. Figure 3 also indicated that the projected area
368 facing flow (YZ_g) of the ganglia-dominated accumulation, rather than γ^g or ganglia mass, was
369 responsible for peak aqueous-phase concentrations. Similarly, Figure 4 shows the projected area
370 YZ_{1A} of the most upgradient, low-saturation accumulation 1A in a high-ranked position. These
371 X_{TCE} results suggested that S_a^N parameters (V_a and $Mass$) of ganglia-dominated accumulations
372 responsible for peak concentrations do not impact TOR when a pool-dominated accumulation is
373 also present; yet their estimation via history-matching may be valuable for remedial designs.
374 Conversely, sensitivity with respect to TOR (X_{TOR}) was dominated by DNAPL pool saturation
375 (S_p^N) parameters, transverse dispersivity ($\alpha_{T,p}$), and depletion exponent (γ^p). The negligible X_{TCE}
376 values of pool parameters suggested difficulty in estimating them from monitoring data alone and
377 value in HRSC for refining characteristic parameters of the pool.

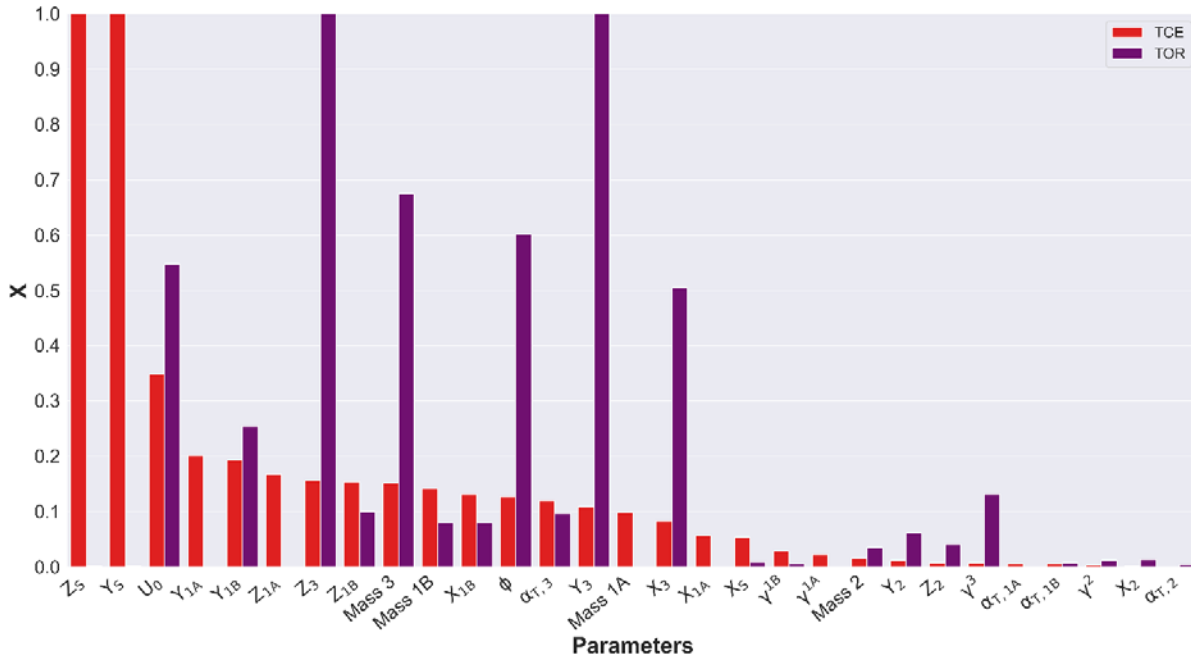
378

379 In contrast to negligible X_{TCE} values by pool parameters in the mixed experiment (Figure 3), X_{TCE}
380 rankings of S_3^N parameters in the heterogeneous experiment (Figure 4) suggested that high-
381 saturation DNAPL accumulations may not exclusively reflect pool fractions of source zones.
382 Typically, the small cross-sectional areas available for dissolution by groundwater flow through
383 DNAPL pools reduces their relative contribution to mass flux, compared to ganglia-dominated
384 accumulations. However, as indicated in Figure 4, the morphology of DNAPL accumulation 3,
385 controlled by flow-field heterogeneity, influenced both X_{TCE} and X_{TOR} rankings in the
386 heterogeneous experiment. The predictive advantage of generalizing mass transfer processes
387 irrespective of S_a^N (Equation 1) over upscaled models predicated on the GTP mass ratio, was
388 further evidenced by a similar effect on X_{TCE} and X_{TOR} incurred by perturbing $\alpha_{T,3}$ (Figure 4).
389 Conversely, the variability of other α_T parameters in both experiments only influenced X_{TOR} .

390



391 **Figure 3.** Sensitivity coefficients with respect to source discharge concentrations measured in the “mixed
 392 architecture” experiment and with respect to the simulated TOR.
 393
 394



395 **Figure 4.** Sensitivity coefficients with respect to source discharge concentrations measured in the “heterogeneous
 396 architecture” experiment and with respect to the simulated TOR.
 397
 398

399 **4.2. Linear Analysis**

400
 401 Prior (σ_{TOR}) and posterior (σ'_{TOR}) standard deviations of TOR uncertainty estimated with FOSM
 402 analysis and mean (μ_{TOR}) values for both experiments are presented in Table 2. Results shown
 403 were calculated using the complete TCE monitoring profiles. As indicated, history-matching
 404 significantly constrained prior TOR uncertainties despite low X_{TCE} values of TOR-sensitive
 405 parameters pertaining to high- S_a^N accumulations.
 406

407

Table 2. Predictive uncertainty of mixed and heterogeneous experiments.

Experiment	μ_{TOR} (days)	σ_{TOR} (days)	σ'_{TOR} (days)
Mixed	27.9	19.8	8.6
Heterogeneous	28.6	20.5	1.7

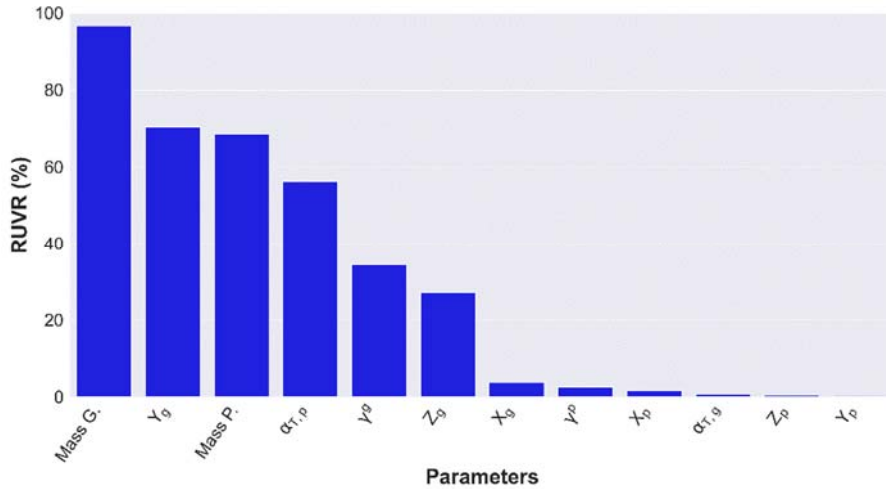
408

409 *4.2.1. Relative Parameter Uncertainty Variance Reduction*

410

411 Figures 5 and 6 show the benefit of history-matching for reducing prior parameter uncertainties.
 412 Despite negligible X_{TCE} values corresponding to the pool mass and $\alpha_{T,p}$ of the mixed experiment
 413 (Figure 3), history-matching reduced the prior uncertainty of these parameters by $\sim 70\%$ and $\sim 60\%$,
 414 respectively (Figure 5). The low uncertainty reduction of γ^p (Figure 5), to which TOR was sensitive
 415 (Figure 3), demonstrated the benefit of coupling upscaled modeling with stochastic analysis tools
 416 for predicting DNAPL longevity timeframes when mass transfer parameters remain unconstrained.
 417 In turn, sensitivity and FOSM analyses of the mixed experiment coincided in a low-ranked $\alpha_{T,g}$,
 418 suggesting that its prior (default) value of 0.001 m is reasonable for simulating dissolution of
 419 ganglia-dominated accumulations.

420



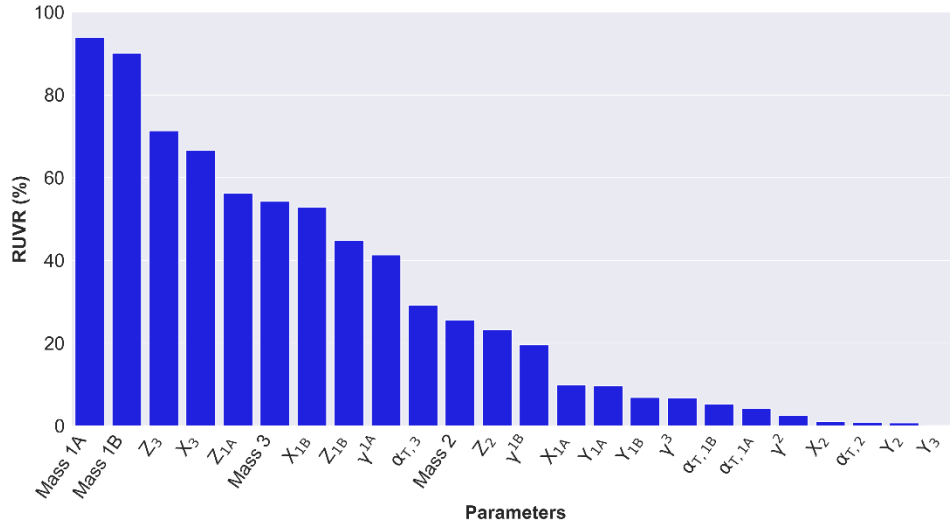
421

422 **Figure 5.** Relative uncertainty variance reduction of VA model parameters of mixed experiment.

423

424 Difficulties in reducing prior uncertainty of the γ parameters in the heterogeneous experiment are
 425 reflected in Figure 6. Yet the prior uncertainty of S_a^N parameters of DNAPL accumulations 1A
 426 (S_{1A}^N), 1B (S_{1B}^N), and 3 (S_3^N) was reduced by approximately more than 50%. The higher RUVR of
 427 S_3^N with respect to other S_a^N parameters was attributed to the sequential dissolution of upgradient
 428 DNAPL masses, allowing the tailing segment of the TCE monitoring profile to constrain the
 429 remaining source architecture (S_3^N). These results implied that modeling efforts supporting the
 430 characterization of sites with aged, pool-dominated source zones, may benefit from history-
 431 matching of monitoring profiles. However, situations with scarce monitoring data and significant
 432 uncertainties on S_a^N distributions along groundwater flow paths may warrant HRSC efforts. In
 433 turn, source characterization data such as DyeLIF and Hydraulic Profiling Tool (HPT) (Horst et
 434 al., 2018) can be leveraged for VA model parameterization, while FOSM analyses can help guide
 435 additional data collection efforts to constrain DNAPL dissolution trends.

436



437 **Figure 6.** Relative uncertainty variance reduction of VA model parameters of heterogeneous experiment.
 438
 439

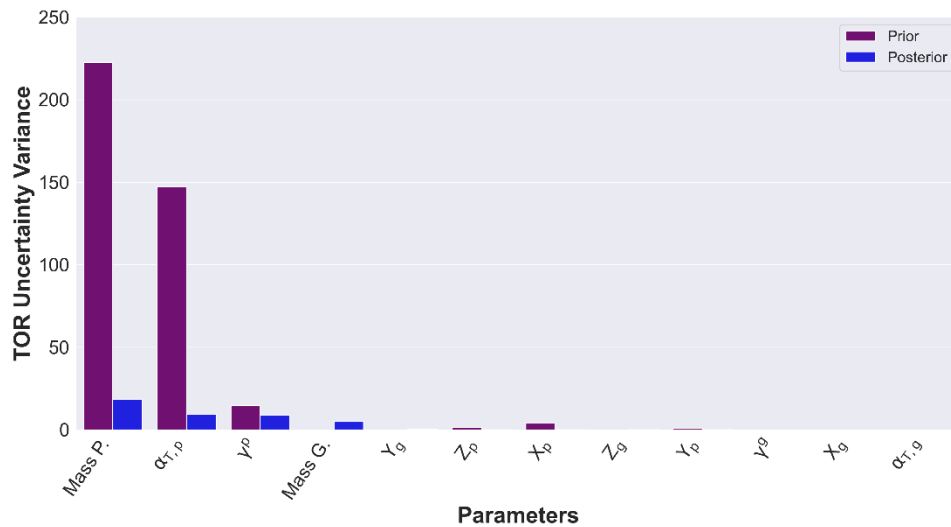
440 *4.2.2. Prior and posterior parameter contributions to predictive uncertainty*
 441

442 As shown in Figure 7, FOSM analyses validated negligible X_{TOR} values caused by the ganglia
 443 parameters in the mixed experiment. Although the pool dispersive area (YX_p) and γ^p influenced
 444 X_{TOR} results (Figure 3), prior and posterior TOR uncertainties of the mixed experiment were clearly
 445 driven by the pool mass and $\alpha_{T,p}$ (Figure 7). Likewise, Figure 8 indicated that the primary drivers
 446 of prior TOR uncertainty in the heterogenous experiment were S_3^N , $\alpha_{T,3}$, and γ^3 . Repeating FOSM
 447 calculations with uncertainty bounds defined as $0 < \alpha_T$ (m) < 0.01 for all DNAPL accumulations
 448 in the heterogeneous experiment did not alter the uncertainty rankings shown in Figure 8. Results
 449 of both experiments agreed on the significance of dispersive mass transfer (α_T) from high-
 450 saturation DNAPL accumulations in regulating TOR. However, the accurate replication of the
 451 heterogenous source dissolution trend with $\alpha_{T,3} = 0$ m was attributed to the contrast in grain sizes,
 452 limiting dispersion from the coarse-grained lenticular zone into the finer surrounding sands despite
 453 high $S_{3,0^N}$ values.

454
 455 Unlike the empirical mass depletion exponent γ^3 , α_T may be directly measured at contaminated
 456 sites to directly constrain mass transfer uncertainties. Examples of field methods include push-pull
 457 tracer tests, borehole and HPT logging, and discrete groundwater sampling with direct push
 458 technology (DPT). These data may be interpreted with 2D analytical modeling (Huang et al.,
 459 2010), grain-size correlations with soil hydraulic conductivity and α_T (Carey et al., 2018), and
 460 spatial moment analysis (Rockhold et al., 2016), respectively. Nonetheless, the α_T component of
 461 DNAPL dissolution expressed in Equation 1 should not be confused with plume-scale
 462 macrodispersion. While dispersivity at the source-zone and plume scales is driven by mechanical
 463 or hydrodynamic mixing along tortuous flow paths (Molz, 2015), coupling a VA model of DNAPL
 464 dissolution with a downgradient contaminant plume model may require two different α_T values
 465 based upon site-specific conditions. Several studies have demonstrated the relationship between
 466 soil grain size and α_T (Carey et al., 2018), concurring with its role on DNAPL mass transfer
 467 (Figures 7 and 8). This is in contrast to Gilland-Sherwood mass transfer correlations which rely
 468 upon aqueous-phase transport models for the contribution of α_T to DNAPL dissolution (Yang et
 469 al., 2019).

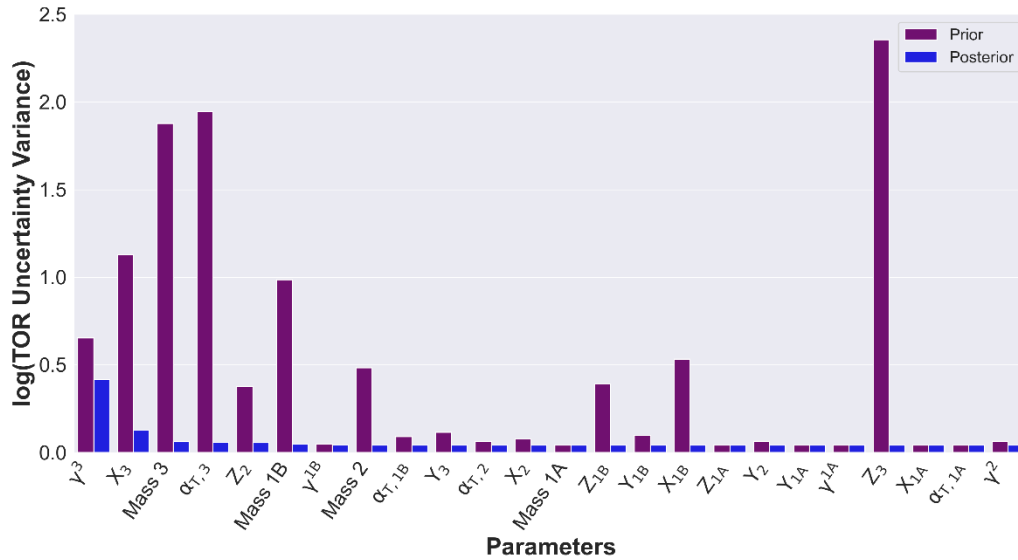
470
471
472
473
474
475
476
477
478
479
480
481
482
483
484

As indicated in Figure 8, the primary driver of posterior TOR uncertainty, γ^3 , reflected its role in regulating source discharge concentrations over several orders of magnitude. While a lack of extensive groundwater monitoring at contaminated sites could limit γ constraining via history-matching, S_a^N and flow-field heterogeneities may also pose additional uncertainties on mass transfer assumptions. In this case, TCE dissolution tailing, primarily regulated by S_3^N , was also modulated by flow channelization in the coarse sand lens (Figure 2b). Transient reductions in DNAPL interfacial areas, which limit mass transfer rates through the γ parameter, were obfuscated by a local increase in U_0 and k_r in the heterogeneous experiment (Stewart et al., 2021). Although the level of characterization detail available for the flow-cell experiment would not be available at field sites, VA modeling provides an efficient means to evaluate conceptual assumptions of system heterogeneities and quantify mass transfer uncertainties. The prior uncertainty rankings of S_{1B}^N and S_3^N parameters (Figure 8) emphasized the level of effort for DNAPL delineation required for adequate model parameterization.



485
486
487

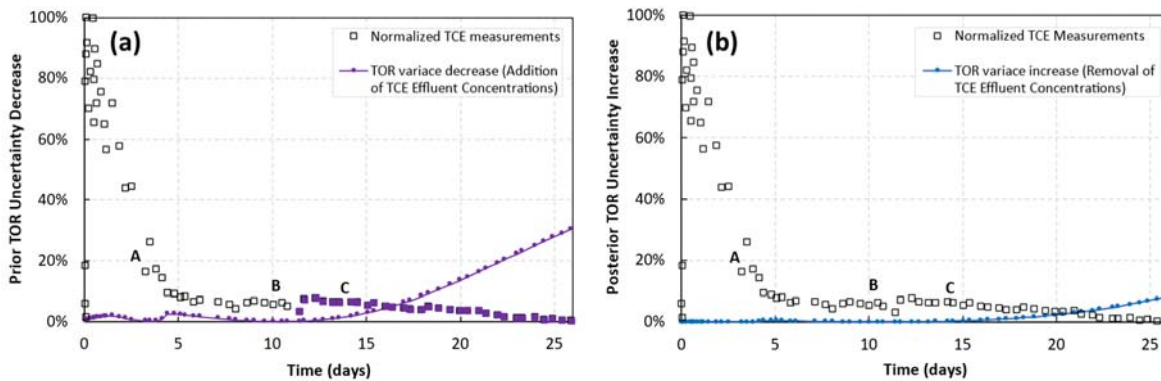
Figure 7. Prior and posterior parameter contributions to TOR uncertainty in the mixed experiment.



488 **Figure 8.** Prior and posterior parameter contributions to TOR uncertainty of heterogeneous experiment.
 489
 490

491 *4.2.3. Data-Worth Analysis*
 492

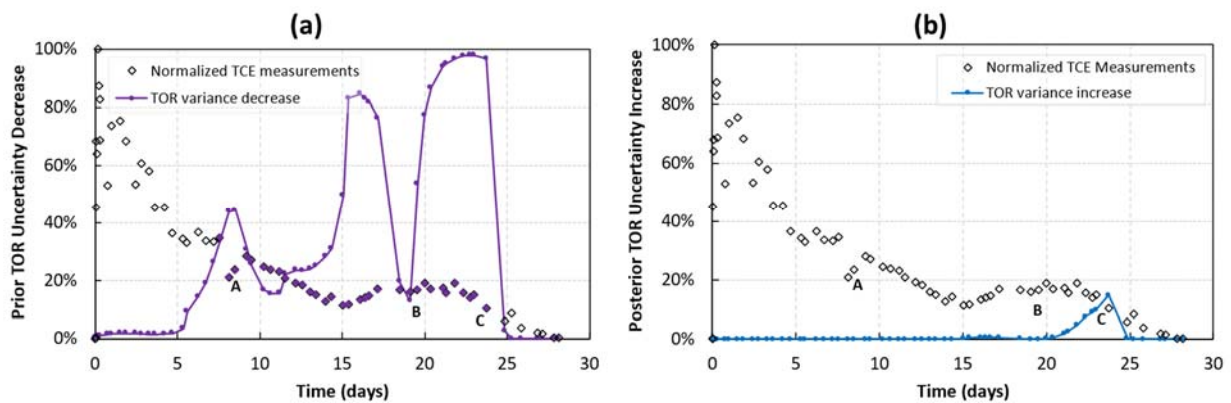
493 The worth of TCE monitoring profiles of the mixed and heterogeneous experiments is shown in
 494 Figures 9 and 10, respectively. Both figures express data worth on the Y-axis as a percent reduction
 495 and increase of σ_{TOR} and σ'_{TOR} (see Table 2), respectively, by individual monitoring
 496 measurements. Figures 9a and 10a indicate the worth of individual measurements for constraining
 497 prior TOR uncertainty (σ_{TOR}), whereas Figures 9b and 10b depict increases in posterior
 498 (constrained) TOR uncertainty (σ'_{TOR}) caused by data removal. As shown in Figure 10, a tendency
 499 of increasing data worth in the mixed experiment started at point C, when the pool mass transfer
 500 area ($A_{p,xy}$) was sufficiently reduced to onset dissolution tailing. Similar prior and posterior data-
 501 worth trends in the mixed experiment suggested that peak concentrations emanating from ganglia-
 502 dominated accumulations do not constrain TOR. In turn, the RUVR of pool mass (~70%) and $\alpha_{T,p}$
 503 (~60%) controlling TOR uncertainty was attributed to TCE monitoring after point C (Figure 9),
 504 highlighting the benefit of history-matching for characterizing sites with aged source zones and
 505 simple architectures. In these experiments, point C represents a rough mid-point for the DNAPL
 506 TOR despite an 80% reduction in the total DNAPL mass.
 507



508 **Figure 9.** Worth of monitoring data for constraining TOR uncertainty of the mixed experiment shown in Figure 2a:
 509 a) Decrease in prior uncertainty with addition of individual TCE concentrations. The filled data points highlight the
 510

511 greatest information content for reducing prior TOR uncertainty. b) Increases in posterior uncertainty with data
 512 removal. Points A, B, C show DNAPL depletion images measured by DiFilippo et al. (2010).

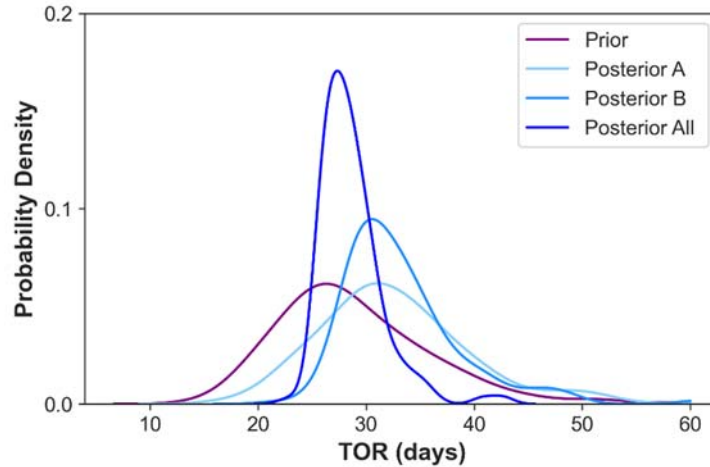
513
 514 Figure 10a shows the worth of breakthrough inflection points along the TCE monitoring curve of
 515 the heterogeneous experiment for constraining σ_{TOR} . The first peak in the σ_{TOR} decrease curve
 516 coincided with point A, indicating the onset of rapid dissolution of DNAPL mass accumulation 1b
 517 after mass 1a was completely dissolved. The second peak of σ_{TOR} reduction occurred during a
 518 slight increase in TCE concentrations, reflecting an increased k_r through mass 2 after mass 1B was
 519 dissolved. The final peaks of σ_{TOR} reduction (Figure 10a) and σ'_{TOR} increase (Figure 10b)
 520 coincided with the final stage of DNAPL dissolution associated to mass 3. These results
 521 highlighted disadvantages of predicting future system behavior from limited monitoring profiles,
 522 corresponding to situations where remaining source architectures and heterogeneities have not yet
 523 been reflected in historical dissolution trends.
 524



525
 526 **Figure 10.** Worth of TCE dissolution measurements for reducing TOR uncertainty of the heterogeneous experiment
 527 shown in Figure 2b: a) Decrease in prior uncertainty with addition of individual history-matching constraints. The
 528 filled data points highlight the greatest information content for reducing prior TOR uncertainty. b) Increases in
 529 posterior uncertainty with data loss. Points A, B, C show the DNAPL depletion measured by DiFilippo et al. (2010).
 530

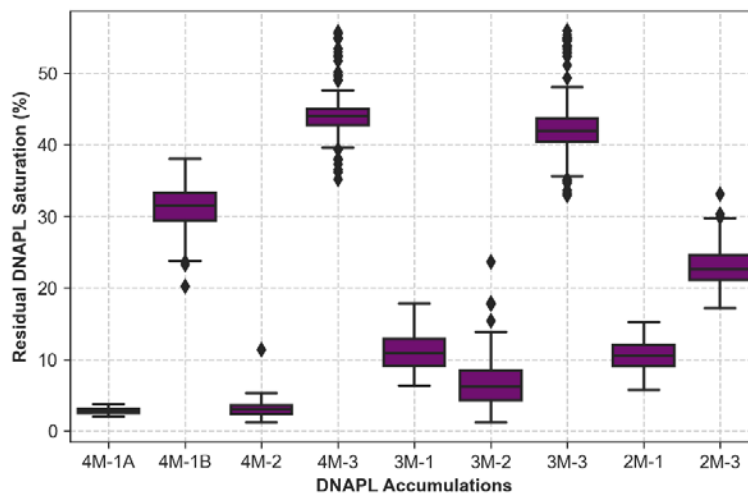
531 **4.3. Nonlinear Uncertainty Analysis**

532
 533 Figure 11 indicates that all prior and posterior source dissipation timeframes of the mixed
 534 experiment included the “true TOR” ($\mu_{TOR} = 27.9$ days). All posterior analyses underestimated the
 535 initial DNAPL mass in the mixed experiment by $\sim 11\%$, yet the known value of 17.2 g was included
 536 within 95% confidence limits (results not shown). The average estimated S_g^N and S_p^N values were
 537 4% and 40%, respectively, consistent with initial experimental conditions (Figure 2a). Prior and
 538 posterior TOR uncertainties in Figure 11 demonstrated the utility of VA modeling for estimating
 539 unbiased depletion timeframes a priori, by leveraging DNAPL-delineation or limited monitoring
 540 data pertaining to source zones with relatively simple architectures and flow conditions.
 541

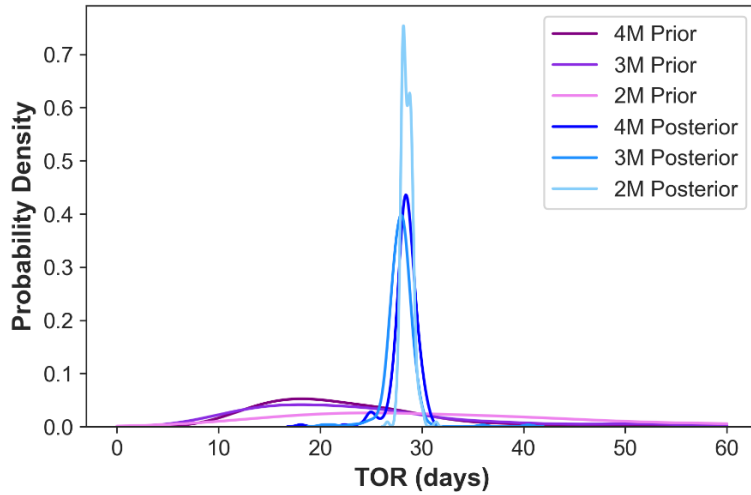


542 **Figure 11.** Prior and posterior TOR PDFs of mixed experiment. Posterior A and B were estimated by history-
 543 matching TCE concentrations through day 11.7 and 20 (Figure 10), respectively.
 544

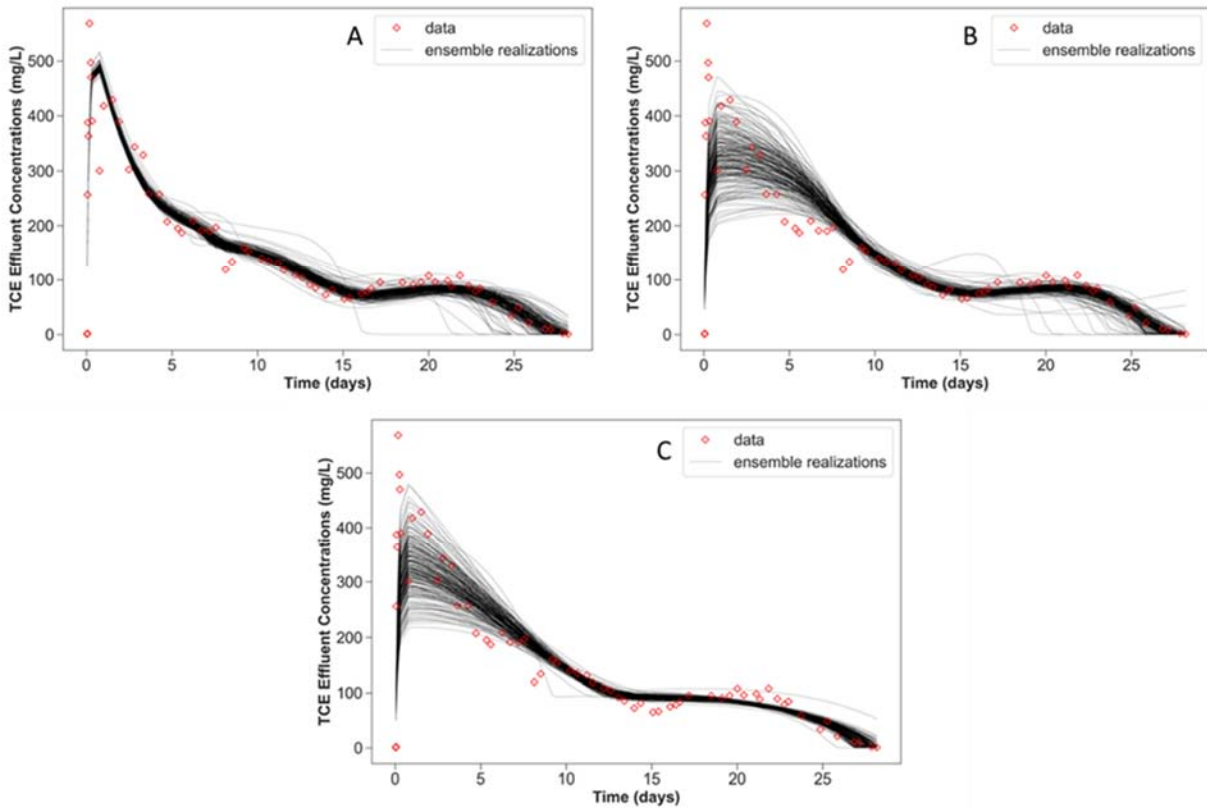
545
 546 The stochastic optimization of the heterogeneous experiment models underestimated initial
 547 DNAPL mass by $\sim 7\%$, with 95% confidence limits encompassing the injected amount of 20.4 g
 548 (results not shown). As illustrated in Figure 12, posterior S_a^N uncertainties reflected the averaging
 549 by model resolutions required to history-match the complete TCE dissolution profile and quantify
 550 TOR uncertainty (Figure 13). Figure 13 shows all posterior TOR PDFs encompassing the “true”
 551 TOR of 28.6 days, emphasizing the worth of final DNAPL dissolution stages for constraining TOR
 552 with various model resolutions. However, the 2M and 3M models required removing peak TCE
 553 concentrations from day 0 through day 9 (Figure 14). Not doing so did not impact the accuracy of
 554 estimated DNAPL mass, but resulted in an artificially low initial S_l^N of lumped mass 1 from
 555 inadequate parameterization complexity (results not shown). Sufficient source architecture
 556 parameters are thereby necessary to assimilate complex dissolution profiles to avoid misleading
 557 injection-based remedial designs.
 558



559 **Figure 12.** Posterior DNAPL saturation distributions of each DNAPL accumulation in the 4M, 3M, and 2M VA
 560 models of the heterogeneous experiment.
 561
 562



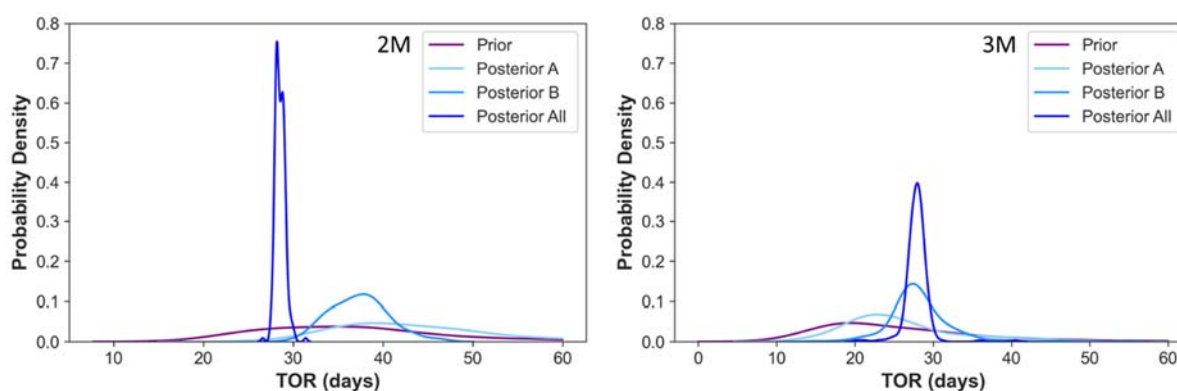
563 **Figure 13.** Prior and posterior TOR PDFs of the heterogeneous experiment conceptualized by 2, 3, and 4 DNAPL
 564 accumulations.
 565
 566
 567



568 **Figure 14.** Posterior model ensembles of the heterogeneous experiment corresponding to (A) 4, (B) 3, and (C) 2
 569 DNAPL accumulations.
 570
 571

572 Figure 15 shows prior predictive PDFs approximated with S_a^N constraints assuming availability of
 573 HRSC data to inform model parameters. The prior S_a^N constraints for this analysis correspond
 574 Figure 12. Despite low probability densities, all prior PDFs encompassed the $\mu_{TOR} = 28.6$ days,
 575 suggesting that even a low-resolution model (2M) accounting for S_a^N distributions along the flow

576 path can predict unbiased source dissipation timeframes. However, Figure 15 depicts biased
 577 posterior 2M PDFs tending to exclude μ_{TOR} resulting from monitoring data assimilation with
 578 inadequate parameterization complexity. Unlike 2M, 3M included an adjustable “dissolution
 579 enhancement factor” representing increased velocity through the coarse lens. Omitting that
 580 parameter from the 3M model (fixing it at a value of 1) did not impact σ'_{TOR} estimated from the
 581 entire TCE profile (Figures 14 and 15). However, σ_{TOR} and σ'_{TOR} estimated from partial TCE
 582 profiles were also overestimated (excluding μ_{TOR}) and the nonmonotonic increase in TCE
 583 concentrations from day 15 through day 20 could not be reproduced (results not shown). Hence,
 584 the unbiased Posterior A and B results of the 3M model, shown in Figure 15, suggested that in
 585 addition to adequate representation of DNAPL distribution along the local flow path,
 586 parameterization of flow field heterogeneity is also necessary to avoid biasing model estimates
 587 through history-matching of multistage and nonmonotonic dissolution profiles.
 588



589
 590 **Figure 15.** Probability density functions of TOR approximated with 2M and 3M models of heterogeneous experiment.
 591 Posterior A and B PDFs were estimated from partial TCE monitoring profiles through day 14 and 20, respectively.
 592

593 5. Conclusions

594
 595 This work demonstrated a practical approach for estimating DNAPL dissolution timeframes
 596 coupling upscaled modeling with uncertainty analysis methods. Assimilation of monitoring data
 597 may induce model predictive bias without sufficient parameterization complexity representing the
 598 DNAPL source, including sequential dissolution of DNAPL accumulations distributed along the
 599 flow path. In both experiments, saturation parameters and transverse dispersion of pool-dominated
 600 DNAPL accumulations controlled the source zone longevity, and were constrained by tailing of
 601 final dissolution stages despite their negligible sensitivity with respect to measured effluent
 602 concentrations. Because the VA model provides TOR as a direct output, FOSM analyses can be
 603 used to guide site characterization efforts to constrain prior, or remaining posterior parameter
 604 uncertainties responsible for predictive TOR and mass discharge/flux uncertainties. As
 605 demonstrated with the heterogeneous source zone experiment, field mapping of aquifer hydraulics,
 606 and/or estimation of source zone architecture using physically-based inversion methods can be
 607 leveraged to refine site conceptual assumptions encapsulated in VA model parameters. This
 608 includes direct constraining of transverse vertical dispersivity at the source zone scale, regardless
 609 of DNAPL saturation, differentiating its contribution to DNAPL dissolution from macrodispersion
 610 at the contaminant plume scale.
 611

612 Local groundwater velocity and source zone dimensions had a prominent impact on mass
613 discharge and DNAPL persistence because of their scaling role on mass transfer processes. Hence,
614 these parameters require constraining by monitoring and site characterization scales, promoting
615 adequate dilution and flow bypassing effects on DNAPL dissolution. Conversely, saturation
616 parameters of ganglia-dominated DNAPL accumulations, which may not be directly measured at
617 field sites, did not impact source longevity timeframes when pools were present. Yet their
618 influence on peak discharge concentrations justifies their parameterization to avoid erroneous
619 estimates of DNAPL saturation distributions and mass discharge rates. Although accurately
620 simulating mass discharge was possible with increased resolution of source zone architecture,
621 exclusive designations of ganglia and pool fractions of DNAPL may be inadequate for mass
622 transfer modeling. The high-saturation DNAPL accumulation embedded in the coarse sand lens of
623 the heterogeneous experiment, controlled the source zone longevity without dispersive mass
624 transfer. Moreover, lumping the downgradient saturations and ignoring flow field heterogeneity,
625 biased lifespan estimates of the heterogenous source zone and degraded the replication of
626 nonmonotonic DNAPL dissolution tailing. While this level of characterization detail may not be
627 available for contaminated sites, upscaled modeling and stochastic uncertainty analyses of site
628 conceptual assumptions can support risk-based decision making through data assimilation and
629 predictive hypothesis testing with a physical mass transfer basis.

630

631 **Acknowledgements**

632

633 This study was supported by the Environmental Security Technology Certification Program
634 (ESTCP) under Project ER19-5223. The content of this manuscript has not been subject to agency
635 review and does not necessarily represent the view of the sponsoring agency.

636

637 **Data Availability Statement**

638

639 A copy of the VA model executable and input instructions can be requested from Praxis
640 Environmental Tech., Inc. at <https://www.praxis-enviro.com/contact>. The SENSAN, PWTADJ2,
641 PREDUNC, GENLINPRED, and PEST software utilities used for sensitivity and linear
642 uncertainty analyses are available at <https://pesthomepage.org/programs>. The PESTPP-iES
643 software used for ensemble-based parameter estimation and nonlinear uncertainty analyses is
644 available at [https://www.usgs.gov/software/pest-software-suite-parameter-estimation-
645 uncertainty-analysis-management-optimization-and](https://www.usgs.gov/software/pest-software-suite-parameter-estimation-uncertainty-analysis-management-optimization-and) (version 5.1.6 was used and the source code
646 is available on <https://github.com/usgs/pestpp/releases/tag/5.1.6>). Except for the data-worth results
647 figures, figures in the results and discussion section were produced with the Matplotlib
648 (<https://matplotlib.org/>) version 3.5.1 and Seaborn (<https://seaborn.pydata.org/>) version 0.11.2
649 libraries using the Python programming language. Data is supplied in an excel file for peer review
650 purposes and will be archived in an online repository maintained by Virginia Tech with a unique
651 DOI number.

652

653

654

655

656

657

658 **6. References**

659

660 Abriola, L. M. (2005). Guest Editorial: Contaminant Source Zones: Remediation or Perpetual
661 Stewardship? *Environmental Health Perspectives*, 113(7), A438-A439.
662 <https://doi.org/10.1289/ehp.113-a438>

663 Abriola, L. M., Miller, E. L., Pennell, K. D., Ramsburg, A., & Christ, J. A. (2013). *Metric*
664 *identification and protocol development for characterizing DNAPL source zone*
665 *architecture and associated plume response*. Alexandria, VA: SERDP Project ER-1612.

666 Agaoglu, B., Coptly, N. K., Scheytt, T., & Hinkelmann, R. (2015). Interphase mass transfer
667 between fluids in subsurface formations: A review. *Advances in Water Resources*, 79, 162-
668 194. <https://doi.org/10.1016/j.advwatres.2015.02.009>

669 Arshadi, M., De Paolis Kaluza, M. C., Miller, E. L., & Abriola, L. M. (2020). Subsurface Source
670 Zone Characterization and Uncertainty Quantification Using Discriminative Random
671 Fields. *Water Resources Research*. <https://doi.org/10.1029/2019WR026481>

672 Carey, G. R., McBean, E. A., & Feenstra, S. (2018). Estimating transverse dispersivity based on
673 hydraulic conductivity. *Environmental Technology & Innovation*, 10, 36-45.
674 <https://doi.org/10.1016/j.eti.2018.01.008>

675 Christ, J. A., Ramsburg, A. C., Pennell, K. D., & Abriola, L. M. (2006). Estimating mass discharge
676 from dense nonaqueous phase liquid source zones using upscaled mass transfer
677 coefficients: An evaluation using multiphase numerical simulations. *Water Resources*
678 *Research*, 42(11). <https://doi.org/10.1029/2006WR004886>

679 Christ, J. A., Ramsburg, C. A., Pennell, K. D., & Abriola, L. M. (2010). Predicting DNAPL mass
680 discharge from pool-dominated source zones. *Journal of Contaminant Hydrology*, 114(1-
681 4), 18 - 34. <https://doi.org/10.1016/j.jconhyd.2010.02.005>

682 Dekker, T. J., & Abriola, L. M. (2000). The influence of field-scale heterogeneity on the infiltration
683 and entrapment of dense nonaqueous phase liquids in saturated formations. *Journal of*
684 *Contaminant Hydrology*, 42(2-4), 187-218. [https://doi.org/10.1016/S0169-](https://doi.org/10.1016/S0169-7722(99)00092-3)
685 [7722\(99\)00092-3](https://doi.org/10.1016/S0169-7722(99)00092-3)

686 DiFilippo, E. L., & Brusseau, M. L. (2008). Relationship Between Mass Flux Reduction and
687 Source-Zone Mass Removal: Analysis of Field Data. *Journal of Contaminant Hydrology*,
688 98(1-2), 22-35. <https://doi.org/10.1016/j.jconhyd.2008.02.004>

689 DiFilippo, E. L., & Brusseau, M. L. (2011). Assessment of a Simple Function to Evaluate the
690 Relationship Between Mass Flux Reduction and Mass Removal for Organic-Liquid
691 Contaminated Source Zones. *Journal of Contaminant Hydrology*, 123(3-4), 104-113.
692 <https://doi.org/10.1016/j.jconhyd.2010.12.011>

- 693 DiFilippo, E. L., Carroll, K. C., & Brusseau, M. (2010). Impact of organic-liquid distribution and
694 flow heterogeneity on reductions in mass flux. *Journal of Contaminant Hydrology*, 115(1-
695 4), 14-25. <https://doi.org/10.1016/j.jconhyd.2010.03.002>
- 696 Doherty, J. (2015). *Calibration and Uncertainty Analysis for Complex Environmental Models*.
697 Brisbane, Australia: Watermark Numerical Computing.
- 698 Doherty, J., & Moore, C. (2020). Decision Support Modeling: Data Assimilation, Uncertainty
699 Quantification, and Strategic Abstraction. *Groundwater*, 58(3), 327-337.
700 <https://doi.org/10.1111/gwat.12969>
- 701 Eniarson, M., Fure, A., St. Germain, R., Chapman, S., & Parker, B. (2018). DyeLIF™: A New
702 Direct-Push Laser-Induced Fluorescence Sensor System for Chlorinated Solvent DNAPL
703 and Other Non-Naturally Fluorescing NAPLs. *Groundwater Monitoring & Remediation*,
704 28-42. <https://doi.org/10.1111/gwmmr.12296>
- 705 Falta, R. (2003). Modeling sub-grid-block-scale dense nonaqueous phase liquid (DNAPL) pool
706 dissolution using a dual-domain approach. *Water Resources Research*, 39(12).
707 <https://doi.org/10.1029/2003WR002351>
- 708 Finsterle, S. (2015). Practical notes on local data-worth analysis. *Water Resources Research*.
709 <https://doi.org/10.1002/2015WR017445>
- 710 Frind, E. O., Molson, J. W., & Schirmer, M. (1999). Dissolution and mass transfer of multiple
711 organics under field conditions: The Borden emplaced source. *Water Resources Research*,
712 35(3), 683-694. <https://doi.org/10.1029/1998WR900064>
- 713 Guo, Z., Russo, A. E., DiFilippo, E. L., Zhang, Z., Zheng, C., & Brusseau, M. L. (2020).
714 Mathematical modeling of organic liquid dissolution in heterogeneous source zones.
715 *Journal of Contaminant Hydrology*, 235. <https://doi.org/10.1016/j.jconhyd.2020.103716>
- 716 Horst, J., Welty, N., Stuetzle, R., Wenzel, R., & Germain, R. (2018). Fluorescent dyes: A new
717 weapon for conquering DNAPL characterization. *Groundwater Monitoring &*
718 *Remediation*, 38(1), 19-25. <https://doi.org/10.1111/gwmmr.12261>
- 719 Huang, J., Christ, J. A., & Goltz, M. N. (2010). Analytical solutions for efficient interpretation of
720 single-well push-pull tracer tests. *Water Resources Research*.
721 <https://doi.org/10.1029/2008WR007647>
- 722 ITRC (Interstate Technology & Regulatory Council). (2010). *Use and Measurement of Mass Flux*
723 *and Mass Discharge*. Washington, D.C.: Interstate Technology & Regulatory Council,
724 Integrated DNAPL Site Strategy Team. Retrieved from www.itrcweb.org
- 725 Kang, X., Kokkinaki, A., Kitandis, P. K., Shi, X., Lee, J., Mo, S., & Wu, J. (2021a).
726 Hydrogeophysical Characterization of Nonstationary DNAPL Source Zones by Integrating
727 a Convolutional Variational Autoencoder and Ensemble Smoother. *Water Resources*
728 *Research*, 57(1). <https://doi.org/10.1029/2020WR028538>

- 729 Kang, X., Kokkinaki, A., Power, C., Kitandis, P. K., Shi, X., Duan, L., . . . Wu, J. (2021b).
730 Integrating deep learning-based data assimilation and hydrogeophysical data for improved
731 monitoring of DNAPL source zones during remediation. *Journal of Hydrology*, *601*,
732 126655. <https://doi.org/10.1016/j.jhydrol.2021.126655>
- 733 Kang, X., Kokkinaki, A., Shi, X., Yoon, H., Lee, J., Kitandis, P. K., & Wu, J. (2022). Integration
734 of Deep Learning-Based Inversion and Upscaled Mass-Transfer Model for DNAPL Mass-
735 Discharge Estimation and Uncertainty Assessment. *Water Resources Research*, *58*(10).
736 <https://doi.org/10.1029/2022WR033277>
- 737 Klenk, I. D., & Grathwohl, P. (2002). Transverse vertical dispersion in groundwater and the
738 capillary fringe. *Journal of Contaminant Hydrology*, *58*(1–2), 111-128.
739 [https://doi.org/10.1016/S0169-7722\(02\)00011-6](https://doi.org/10.1016/S0169-7722(02)00011-6)
- 740 Koch, J., & Nowak, W. (2015). Predicting DNAPL mass discharge and contaminated site
741 longevity probabilities: Conceptual model and high-resolution stochastic simulation.
742 *Water Resources Research*, 806 - 831. <https://doi.org/10.1002/2014WR015478>.
- 743 Koch, J., & Nowak, W. (2016). Identification of contaminant source architectures—A statistical
744 inversion that emulates multiphase physics in a computationally practicable manner. *Water*
745 *Resources Research*, *52*, 1009–1025. <https://doi.org/10.1002/2015WR017894>
- 746 Kokkinaki, A., O'Carroll, M., Werth, C. J., & Sleep, B. E. (2013). Coupled simulation of DNAPL
747 infiltration and dissolution in three-dimensional heterogeneous domains: Process model
748 validation. *Water Resources Research*, *49*, 7023-7036.
749 <https://doi.org/10.1002/wrcr.20503>, 2013
- 750 Kokkinaki, A., Werth, C. J., & Sleep, B. E. (2014). Comparison of upscaled models for multistage
751 mass discharge from DNAPL source zones. *Water Resources Research*, 3187 - 3205.
752 <https://doi.org/10.1002/2013WR014663>
- 753 Kueper, B. H., Stroo, H. F., Vogel, C. M., & Ward, C. H. (2014). *Chlorinated Solvent Source Zone*
754 *Remediation*. Springer New York. <https://doi.org/10.1007/978-1-4614-6922-3>
- 755 Lemke, L. D., & Abriola, L. M. (2006). Modeling dense nonaqueous phase liquid mass removal
756 in nonuniform formations: Linking source-zone architecture and system response.
757 *Geosphere*, *2*(2), 74-82. <https://doi.org/10.1130/GES00025.1>
- 758 Marble, J. C., DiFilippo, E. L., Zhang, Z., Tick, G. R., & Brusseau, M. L. (2008). Application of
759 a lumped-process mathematical model to dissolution of non-uniformly distributed
760 immiscible liquid in heterogeneous porous media. *Journal of Contaminant Hydrology*,
761 *100*, 1-10. <https://doi.org/10.1016/j.jconhyd.2008.04.003>
- 762 Miller, C. T., Christakos, G., Imhoff, P. T., McBride, J. F., & Pedit, J. A. (1998). Multiphase flow
763 and transport modeling in heterogeneous porous media: challenges and approaches.
764 *Advances in Water Resources*, *21*(2), 77-120. [https://doi.org/10.1016/S0309-](https://doi.org/10.1016/S0309-1708(96)00036-X)
765 [1708\(96\)00036-X](https://doi.org/10.1016/S0309-1708(96)00036-X)

- 766 Mobile, M. A., Widdowson, M. A., & Gallagher, D. L. (2012). Multicomponent NAPL Source
767 Dissolution: Evaluation of Mass-Transfer Coefficients. *Environmental Science &*
768 *Technology*, 46(18), 10047-10054. <https://doi.org/10.1021/es301076p>
- 769 Molz, F. (2015). Advection, Dispersion, and Confusion. *Ground Water*, 53(3), 348-353.
770 <https://doi.org/10.1111/gwat.12338>
- 771 Moore, C., & Doherty, J. (2005). Role of the calibration process in reducing model predictive
772 error. *Water Resources Research*. <https://doi.org/10.1029/2004WR003501>
- 773 Parker, J. C., & Park, E. (2004). Modeling field-scale dense nonaqueous phase liquid dissolution
774 kinetics in heterogeneous aquifers. *Water Resources Research*, 2004.
775 <https://doi.org/10.1029/2003WR002807>
- 776 Powers, S. E., Abriola, L. M., & Weber Jr, W. J. (1992). An Experimental Investigation of
777 Nonaqueous Phase Liquid Dissolution in Saturated Subsurface Systems: Steady State Mass
778 Transfer Rates. *Water Resources Research*, 28(10), 2691-2705.
779 <https://doi.org/10.1029/92WR00984>
- 780 Powers, S. E., Abriola, L. M., & Weber, W. J. (1994). An experimental investigation of
781 nonaqueous phase liquid dissolution in saturated systems: Transient mass transfer rates.
782 *Water Resources Research*, 30(2), 321-332. <https://doi.org/10.1029/93WR02923>
- 783 Rockhold, M., Zhang, Z., & Bott, Y.-J. (2016). *Scale-Dependent Solute Dispersion in Variably*
784 *Saturated Porous Media*. Richland, WA: Pacific Northwest National Laboratory.
- 785 Saenton, S., & Illangasekare, T. H. (2004). Determination of DNAPL entrapment architecture
786 using experimentally validated numerical codes and inverse modeling. *Developments in*
787 *Water Science*, 55, 767-778. [https://doi.org/10.1016/S0167-5648\(04\)80098-4](https://doi.org/10.1016/S0167-5648(04)80098-4)
- 788 Saenton, S., & Illangasekare, T. H. (2007). Upscaling of mass transfer rate coefficient for the
789 numerical simulation of dense nonaqueous phase liquid dissolution in heterogeneous
790 aquifers. *Water Resources Research*, 43(2). <https://doi.org/10.1029/2005WR004274>
- 791 Stewart, L. D., Chambon, J. C., Widdowson, M. A., & Kavanaugh, M. C. (2022). Upscaled
792 modeling of complex DNAPL dissolution. *Journal of Contaminant Hydrology*, 244.
793 <https://doi.org/10.1016/j.jconhyd.2021.103920>
- 794 Tang, T. (2019). *An Adjoint-Sensitivity-Analysis Based Mathematical Framework: DNAPL Source*
795 *Zone Characterization, Uncertainty Quantification, and Sampling Strategy Design*
796 (Doctoral dissertation). Civil and Environmental Engineering. Ann Arbor, MI: Tufts
797 University. Retrieved from ProQuest (Access provided by University Libraries through
798 Virginia Tech)
- 799 Watermark Numerical Computing. (2018). *Model-Independent Parameter Estimation. User*
800 *Manual Part II: PEST Utility Support Software*.
- 801 White, J. T. (2018). A model-independent iterative ensemble smoother for efficient history-
802 matching and uncertainty quantification in very high dimensions. *Environmental*

